Joint Range and Doppler Estimation Using Spectrally Efficient FDM

Michele Mirabella, *Member, IEEE*, Pasquale Di Viesti, *Member, IEEE*, Christos Masouros, *Fellow, IEEE*, and Giorgio M. Vitetta, *Senior Member, IEEE*

***Abstract*—This paper explores the use of data modulated by a spectrally efficient frequency division multiplexing (SEFDM) waveform for sensing. We first show that, if the presence of a cyclic prefix is assumed in the transmitted signal, the problem of multiple target sensing is tantamount to the detection and estimation of an unknown number of complex two-dimensional complex tones. Then, a novel iterative estimation method, based on a maximum likelihood approach, is developed to solve the last problem. Our simulation results evidence that SEFDM represents a valid technical option over static or slowly varying channels, and that the proposed method achieves a better accuracy-complexity trade-off than other estimation techniques available in the technical literature. In particular, our numerical results show that, in various scenarios, the proposed method achieves a 15%–50% improvement in estimation accuracy with respect to other techniques with a limited computational complexity.**

***Index Terms*—Cyclic prefix, maximum likelihood estimation, orthogonal frequency division multiplexing, spectral efficiency, radar processing.**

I. Introduction

WIRELESS communication and radar sensing have been advancing independently for many years, despite sharing various similarities in terms of both signal processing and system architecture. In the last few years, substantial research efforts have been devoted to the design of wireless systems able to perform *communication and radar* functions jointly. The interest in such a class of systems, that accomplish *integrated sensing and communication* (ISAC), has been motivated by the advantages they offer in terms of device size, power consumption, cost and *spectral efficiency* (SE) with respect to traditional wireless systems in various applications [1]. A crucial challenge in ISAC is the design of waveforms allowing to achieve good performance in both communication and sensing under specific spectral and complexity constraints [2]. In this context, one of the available (and underexplored) options is represented by *spectrally efficient frequency division multiplexing* (SEFDM) [3], a modulation format closely related to *orthogonal frequency division multiplexing* (OFDM). In fact, similarly to OFDM, the SEFDM format puts into practice the frequency multiplexing concept by employing multiple subcarriers; however, unlike OFDM, it improves SE by giving up the orthogonality constraint, i.e., by increasing the spectral overlap among distinct subcarriers, to allow more subcarriers in a given bandwidth. Unfortunately, this advantage is obtained at the price of the unavoidable introduction of *inter-carrier interference* (ICI) at the *receive* (RX) side and, consequently, of a higher data detection complexity. This has motivated the interest in developing computationally efficient detection and decoding techniques for mitigating the impact of ICI in SEFDM communication systems [4], [5], [6], [7], [8]. Note that all these contributions address the problem of data detection in SEFDM from a communication perspective; in this manuscript, instead, we focus on the use of SEFDM signaling for wireless sensing, i.e., for estimating the range and radial speed of multiple targets in place of the data symbols conveyed by the radiated waveform.

While the use of the orthogonal counterpart of SEFDM (namely, OFDM) has received significant attention in ISAC (e.g., see [1], [2], [9], [10], [11], [12], [13], [14], [15], [16]), no attention has been paid to the adoption of SEFDM for similar purposes. Among these contributions, the work in [16] offers an overview of *single-input single-output* (SISO) OFDM radar techniques for target estimation, providing a unified perspective on existing methods. In contrast, the present work explores SEFDM from a sensing perspective, with the aim of partially filling this knowledge gap. In particular, we analyze its potential as a radar waveform and assess the inherent trade-off between sensing performance and communication efficiency according to the amount of compression introduced in subcarrier spacing.

It is also worth mentioning that target detection and estimation algorithms developed for passive sensing in OFDM-based systems can be divided into *direct* and *indirect* methods. In general, direct sensing methods estimate radar target parameters directly from the RX signal without compensating for the communication payload. These approaches often rely on computationally intensive *compressed sensing* techniques [1]. Conversely, indirect sensing methods require an initial estimation of the communication channel, which is then used to subtract the contribution of the transmitted data

Received 4 July 2025; revised 19 September 2025; accepted 23 January 2026. Date of publication 4 February 2026; date of current version 5 February 2026. This work was supported in part by European Union through Italian National Recovery and Resilience Plan (PNRR); in part by the "Telecommunications of the Future" Partnership [PE00000001—program RESearch and innovation on future Telecommunications systems and networks (RESTART)], D.D. n.1549 of 11/10/2022 and within the initiatives of Mission 4 Component 2, Investment 1.4 (D.D. 1033 17/06/2022, CN00000023) under Grant CUP E63C22002040007;and in part by the project the MOST–Sustainable Mobility National Research Center. The associate editor coordinating the review of this article and approving it for publication was X. Li. *(Corresponding author: Michele Mirabella.)*

Michele Mirabella, Pasquale Di Viesti, and Giorgio M. Vitetta are with the Department of Engineering "Enzo Ferrari," University of Modena and Reggio Emilia, 41125 Modena, Italy, and also with the Consorzio Nazionale Interuniversitario per le Telecomunicazioni (CNIT), 43124 Parma, Italy (e-mail: michele.mirabella@unimore.it; pasquale.diviesti@unimore.it; giorgio.vitetta@unimore.it).

Christos Masouros is with University College London, WC1E 7JE London, U.K. (e-mail: c.masouros@ucl.ac.uk).

Digital Object Identifier 10.1109/TWC.2026.3658942

symbols (e.g., see [9, Eq. (20)]). Indirect methods can be further categorized into: 1) *discrete Fourier transform* (DFT)-based or correlation-based methods [10]; 2) subspace methods [11], [12]; 3) *maximum likelihood* (ML)-based methods [13], [14]. A common feature across the aforementioned techniques is the use of an initial coarse estimate (typically obtained through the *periodogram method* applied to *range-Doppler* maps [15]), whereas the main differences among them concern their refinement stage, where different signal processing techniques are used to improve the target initial estimates.

This paper is motivated by our interest in investigating the use of SEFDM for radio sensing. For this reason, we explore its application to the detection and estimation of multiple targets, both in range and Doppler, within an ISAC framework.

The scope of this manuscript is threefold. First, we develop a simplified model for the received signal in a co-located SISO SEFDM transceiver. In doing so, we account for the presence of a *cyclic prefix* (CP), typically overlooked in SEFDM studies, in the transmitted signal. Note that incorporating a CP eliminates *inter-symbol interference* (ISI), significantly easing channel estimation at the price of reduced SE. Second, we exploit the above-mentioned signal model and develop a novel approximate ML-based method for the detection and estimation of multiple targets. This method, dubbed *Newton-based multiple cisoid refiner* (NMCR), combines a coarse initialization based on the periodogram method with a Newton-based iterative refinement strategy that jointly optimizes target parameters (for this reason, it belongs to the class of indirect sensing techniques). Thirdly, we assess the accuracy and computational requirements of the NMCR method in multiple heterogeneous scenarios and we compare it with other methods available in the technical literature. Our numerical results lead to the conclusion that, in various scenarios, the NMCR can achieve 15%–50% improvement in estimation accuracy with respect to other techniques with reasonable complexity.

The remaining part of this manuscript is organized as follows. In Section II, the processing accomplished in a SEFDM-based radar system is described, a simplified model is developed for the received signal feeding the NMCR algorithm and, based on this model, a simple method for the estimation of the channel matrix is proposed. Section III is devoted to the derivation of the NMCR algorithm and to the assessment of its computational complexity. The NMCR algorithm is compared, in terms of accuracy and complexity, with other estimation algorithms in Section IV. Finally, some conclusions are offered in Section V.

Notation: Throughout this manuscript, the following notation is adopted:

1) $(\cdot)^*$ and $(\cdot)^H$ denote the complex conjugate and the complex conjugate transpose (Hermitian operator), respectively;

2) $\mathrm{mod}_B[\cdot]$ indicates the *modulo* B operator (where B is a positive integer);

3) $*$ denotes the linear convolution operator between two signals or functions;

4) $\Re\{x\}$ and $\Im\{x\}$ indicate the *real part* and *imaginary part*, respectively, of the complex variable x;

5) The symbols $\odot$ and $\oslash$ represent the *Hadamard product* and *Hadamard division* operators, respectively;

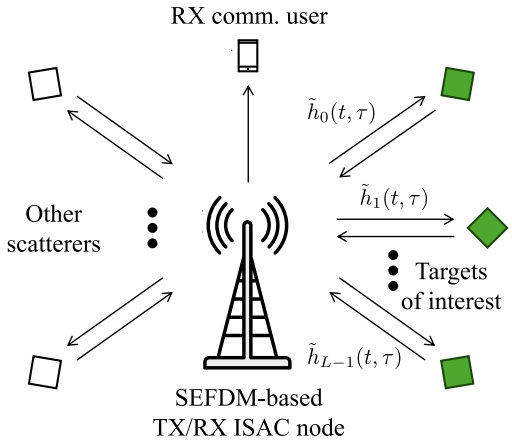

Fig. 1. Representation of the sensing scenario in a SEFDM-based ISAC system. In this case, sensing is accomplished by a wireless node that can establish a communication link with one or multiple users. The presence of targets of interests and other passive targets (scatterers) is explicitly indicated.

6) The symbol $\circledast$ denotes the *Khatri-Rao product* operator;

7) $\mathbf{\Xi}_V$ is the unitary DFT matrix of order V, whose element (p,q) is $\exp(-j2\pi pq/V)/\sqrt{V}$;

8) $\mathbf{X} \triangleq [x_{m,n}]$ defines a matrix $\mathbf{X}$ of proper size and $x_{m,n}$ denotes the element appearing on its mth row and nth column;

9) $\mathbf{y} = \mathrm{vec}(\mathbf{Y})$ defines an (MN)-dimensional column vector resulting from the ordered concatenation of the columns of the $M \times N$ matrix $\mathbf{Y}$;

10) $\mathbf{I}_N$ is the identity matrix of order N;

11) $\mathrm{diag}(\mathbf{x}_N)$ generates a diagonal $N \times N$ matrix having the elements of the N-dimensional vector $\mathbf{x}_N$ on its main diagonal;

12) $\mathbf{Y}^\dagger \triangleq (\mathbf{Y}^H\mathbf{Y})^{-1}\mathbf{Y}^H$ is the *Moore-Penrose pseudo-inverse* of matrix $\mathbf{Y}$;

13) $\mathrm{Tr}\{\mathbf{Y}\}$ defines the *trace* of the matrix $\mathbf{Y}$.

II. System and Signal Models

In this section, the overall processing required for the sensing task in a SISO SEFDM-based ISAC system is briefly described; in doing so, emphasis is put on the processing at the RX side (which coincides with the *transmit*, TX, one in a co-located system). For better clarity, our description is divided into two parts. In the first part, the mathematical model of the received signal in the presence of multiple targets is developed and some essential assumptions on which it relies are illustrated. In the second part, instead, we show how channel estimation can be performed at the TX side of the system; this is then used to generate the signal to be employed for target detection and estimation.

A. Received Signal in the Presence of Multiple Targets

In the following, we take into consideration the transmission of a single SEFDM frame, consisting of M consecutive SEFDM symbols, over a slowly varying wireless channel. We assume that the SEFDM frame incorporates both pilot tones (for channel estimation and synchronization in digital communications) and information data to be sent to a single or multiple receivers at different locations. However, since the receiver is assumed to be co-located with the transmitter

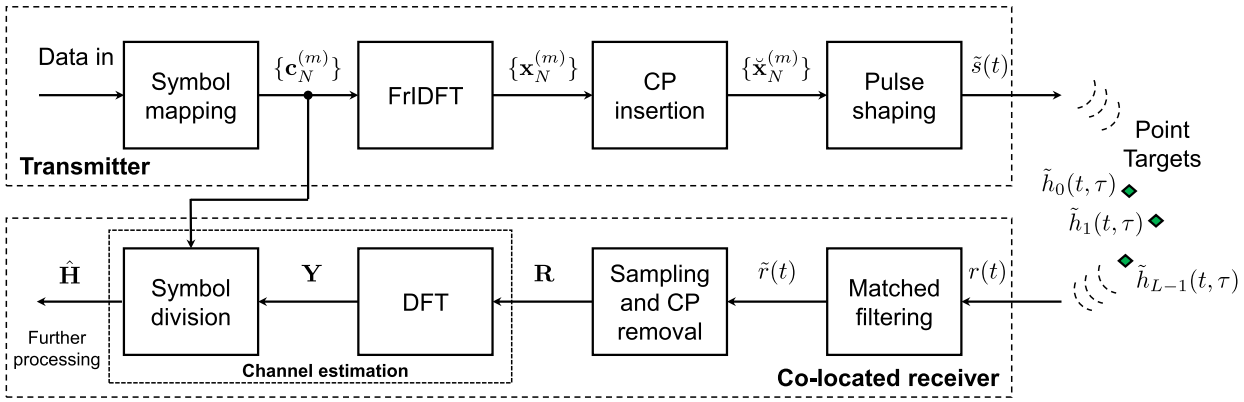

Fig. 2. Baseband architecture of the considered SEFDM-based co-located radar system.

(i.e., *monostatic* sensing is employed), full knowledge of the structure and content of the whole frame, and of the transmission frequency is available at the RX side; this information is exploited by the SEFDM-based ISAC receiver for sensing purposes only, as shown in Fig. 1. Note that, in the following, we focus on a SISO radar architecture employed for estimating the range and Doppler of multiple targets and assume perfect timing synchronization at the RX side.[1] The exact spatial localization of the detected targets would require the adoption of *multiple-input multiple output* (MIMO) radar; however, this issue is out of the scope of this manuscript.

In the following, we also assume that:

1) The mth transmitted SEFDM symbol (with $m = 0, 1, \ldots, M-1$) conveys the N-dimensional vector $\mathbf{c}_N^{(m)} \triangleq [c_0^{(m)}, c_1^{(m)}, \ldots, c_{N-1}^{(m)}]^T$, containing N_u channel symbols (which belong to an M_c-ary constellation) and $(N-N_\mathrm{u})$ zeros (associated with the suppressed subcarriers).[2]

2) Each SEFDM symbol contains a CP having size N_cp, lasting T_cp s, and whose presence guarantees the absence of ISI among adjacent SEFDM symbols.

3) The same subcarrier compression parameter $0 < \beta \leq 1$, which is used to characterize the compression of the spectrum occupied by the N subcarriers compared to OFDM, is adopted for all the SEFDM symbols.

4) The spectrum $P(f)$ of the pulse shaping filter, having *impulse response* (IR) $p(t)$, used in the signal generation stage corresponds to a *root of a raised cosine* (RRC) filter with *roll-off* factor α.

5) At the RX side, a filter matched to $p(t)$ is employed.

The baseband architecture of the SEFDM-based radar system considered in this manuscript is illustrated in Fig. 2.

Our derivation of the SEFDM signal model parallels that provided in [17, Sec. II-A] for a single OFDM symbol. The main difference is represented by the fact that the vector $\mathbf{c}_N^{(m)}$ undergoes an order N *fractional inverse discrete Fourier transform* (FrIDFT) of positive parameter $\beta \leq 1$ (note that, if $\beta = 1$, SEFDM coincides with OFDM); this produces the N-dimensional vector

$$\mathbf{x}_N^{(m)} \triangleq \left[x_0^{(m)}, x_1^{(m)}, \ldots, x_{N-1}^{(m)}\right]^T = \mathbf{F}_{N,\beta}^H \, \mathbf{c}_N^{(m)}, \qquad (1)$$

where $\mathbf{F}_{N,\beta}$ is a square matrix of order N, whose (p,q)th element is equal to $\exp(-j2\pi pq\beta/N)/\sqrt{N}$. Then, $\mathbf{x}_N^{(m)}$ is cyclically extended through a CP; for any m, the first N_cp elements of the resulting $(N+N_\mathrm{cp})$-dimensional vector $\breve{\mathbf{x}}_N^{(m)}$ are generated as $\breve{x}_k^{(m)} = x_{\mathrm{mod}_N[k]}^{(m)}$, with $k \in \{-N_\mathrm{cp}, -N_\mathrm{cp}+1, \ldots, -1\}$.

Under the above assumptions, the complex envelope of the transmitted signal for the considered SEFDM frame can be expressed as (e.g., see [10, Eq. (1)] for OFDM)

$$\tilde{s}(t) = \sum_{m=0}^{M-1} s\left(t - mT, \mathbf{x}_N^{(m)}\right), \qquad (2)$$

where (see [8, Eq. (2)] and the related comments)

$$s(t, \mathbf{x}_N) \triangleq \sum_{k=-N_\mathrm{cp}}^{N-1} x_k \, p(t - kT_\mathrm{s}/\beta), \qquad (3)$$

$T \triangleq NT_\mathrm{s}/\beta$ and T_s is the *channel symbol interval*. The signal in (2) is transmitted over a multipath fading channel, where multiple propagation paths arise due to reflections from L point-like objects in the environment. Among these reflectors, some may correspond to actual targets of interest, while others act as passive scatterers that contribute to the overall channel response (e.g., see Fig. 1). The resulting *channel impulse response* (CIR) is

$$h(t,\tau) \triangleq \sum_{l=0}^{L-1} \tilde{h}_l(t,\tau), \qquad (4)$$

where

$$\tilde{h}_l(t,\tau) \triangleq a_l \, \exp(j2\pi\nu_l t) \, \delta(\tau - \tau_l) \qquad (5)$$

represents the CIR component associated with the lth target (characterized by the gain a_l, the delay τ_l and the Doppler shift ν_l). In the following, we assume that: a) the CIR components are organized according to increasing delays, so that τ_0 and τ_{L-1} represent the minimum and maximum delays, respectively; b) the parameters a_l, τ_l and ν_l do not change over the entire frame (quasi-static channel). Note that, in this context, the delay τ_l and Doppler shift ν_l can be related to the physical parameters of the lth target, namely its range R_l and radial velocity v_l, since $\tau_l \triangleq 2R_l/c$ and $\nu_l \triangleq 2f_\mathrm{c}\, v_l/c$, where c denotes the speed of light and f_c the carrier frequency.

Let us derive now the expression of the matched filter output at the RX side when this filter is fed by $r(t)$, i.e., the channel

[1]The presence of a frequency offset does not represent a technical problem in this case, thanks to the fact that the TX and RX sides are co-located.

[2]Some subcarriers are deliberately suppressed to avoid out-of-band emissions, reduce interference with adjacent channels, and comply with pulse shaping constraints. Their use, as indicated in [17, Sec. II.A], notably simplifies receiver structure.

response to $\tilde{s}(t)$ (2). To simplify our developments, we first evaluate the response

$$\tilde{r}_l(t) \triangleq \tilde{s}(t) * \tilde{h}_l(t,\tau) * p^*(-t), \tag{6}$$

which is obtained when the lth target only is active (so that the CIR is given by $\tilde{h}_l(t,\tau)$ (5)) and channel noise is negligible; then, we account for the presence of multiple targets by summing over l and adding the noise contribution.

Following a similar approach as that illustrated in [16, Sec. II,Eqs. (4)-(7)], it can be proved that

$$\tilde{r}_l(t) = \sum_{m=0}^{M-1} \bar{r}_{l,m}(t) \tag{7}$$

for $t \in (mNT_\mathrm{s}, (m+1)NT_\mathrm{s})$, with $m = 0, 1, \ldots, M-1$; here,

$$\bar{r}_{l,m}(t) = \frac{\beta}{\sqrt{N}T_\mathrm{s}} \tilde{a}_l \sum_{n=0}^{N-1} \bar{x}_n^{(m)} P(\phi_n) P^*(\phi_n - \nu_l) \cdot \exp\big(j2\pi\phi_n(t-\tau_l)\big) \exp(j2\pi\nu_l t), \tag{8}$$

represents the contribution of the mth SEFDM symbol, $\phi_n \triangleq n\beta\Delta_f$, $\Delta_f \triangleq 1/(NT_\mathrm{s})$ is the *subcarrier spacing*, $\tilde{a}_l \triangleq a_l \exp(-j2\pi\nu_l\tau_l)$ and $\bar{x}_n^{(m)}$ is the nth element of the order N DFT of $\mathbf{x}_N^{(m)}$

$$\bar{\mathbf{x}}_N^{(m)} \triangleq \mathrm{DFT}_N[\mathbf{x}_N^{(m)}] = \boldsymbol{\Xi}_N \mathbf{x}_N^{(m)}. \tag{9}$$

The signal $\tilde{r}_l(t)$ (7) is sampled at the instant $t_{m,\tilde{n}} \triangleq \tau_{L-1} + \tilde{n}T_\mathrm{s}/\beta + mNT'$, with $\tilde{n} = 0, 1, \ldots, N + N_\mathrm{cp} - 1$ and $T' \triangleq (T_\mathrm{s} + T_\mathrm{cp})/\beta$. Then, the resulting sequence $\{\tilde{r}_{l,m,\tilde{n}} \triangleq \tilde{r}_l(t_{m,\tilde{n}})\}$ undergoes CP removal; this produces the new sequence $\{r_{l,m,\tilde{n}}\}$, with

$$r_{l,m,\tilde{n}} = \breve{a}_l \sum_{n=0}^{N-1} \bar{x}_n^{(m)} \exp(-j2\pi n f_{\tau_l}) \exp\left(j2\pi n \frac{\tilde{n}}{N}\right) \cdot d_{\tilde{n}}(f_{\nu_l}) \exp\big(j2\pi m f_{\nu_l}\big). \tag{10}$$

In the last expression,

$$\breve{a}_l \triangleq a_l \exp(-j2\pi N f_{\nu_l} f_{\tau_l})/\sqrt{N}, \tag{11}$$

$$f_{\tau_l} \triangleq \beta \frac{\tau_l - \tau_{L-1}}{NT_\mathrm{s}} \tag{12}$$

and

$$f_{\nu_l} \triangleq \frac{\nu_l}{\beta\Delta_f} \tag{13}$$

are the complex gain, the *normalized delay* and *normalized Doppler frequency*, respectively, associated with the lth target, and

$$d_{\tilde{n}}(f_{\nu_l}) \triangleq \exp\left(j2\pi\tilde{n}\frac{f_{\nu_l}}{N}\right) \tag{14}$$

represents a phase rotation, proportional to the sample index $\tilde{n}$ and to the normalized Doppler frequency, associated with the lth target. For a given l, the samples $\{r_{l,m,\tilde{n}}\}$ are stored in the $M \times N$ matrix[3]

$$\mathbf{R}_l \triangleq [r_{l,m,\tilde{n}}] = (\mathbf{X} \odot \mathbf{H}_l)\, \boldsymbol{\Xi}_N^H\, \mathbf{D}_l, \tag{15}$$

where

$$\mathbf{X} \triangleq \big[\bar{\mathbf{x}}_N^{(0)}, \bar{\mathbf{x}}_N^{(1)}, \ldots, \bar{\mathbf{x}}_N^{(M-1)}\big]^T \tag{16}$$

is the $M \times N$ matrix collecting all the channel symbols transmitted within a frame (see (9)), $\mathbf{H}_l \triangleq [H_{l,m,\tilde{n}}]$ is an $M \times N$ channel matrix, with

$$H_{l,m,n} \triangleq \breve{a}_l \exp(-j2\pi n f_{\tau_l}) \exp\big(j2\pi m f_{\nu_l}\big) \tag{17}$$

for any m and n, $\mathbf{D}_l \triangleq \mathrm{diag}(\mathbf{d}_l)$ is an $N \times N$ matrix and

$$\mathbf{d}_l \triangleq [d_0(f_{\nu_l}), d_1(f_{\nu_l}), \ldots, d_{N-1}(f_{\nu_l})]^T \tag{18}$$

is a N-dimensional vector, whose $\tilde{n}$th element is expressed by (14).

Finally, the overall RX signal matrix is obtained by summing the contributions that originate from all the point targets and including the contribution of channel noise; this produces the $M \times N$ matrix

$$\mathbf{R} \triangleq \sum_{l=0}^{L-1} \mathbf{R}_l + \mathbf{W} = \sum_{l=0}^{L-1} (\mathbf{X} \odot \mathbf{H}_l)\, \boldsymbol{\Xi}_N^H\, \mathbf{D}_l + \mathbf{W}, \tag{19}$$

where $\mathbf{W} \triangleq [w[m,n]]$ is the $M \times N$ matrix representing the contribution of channel noise; in the following, it is assumed that the elements of $\mathbf{W}$ are *independent and identically distributed* (i.i.d.) complex Gaussian random variables.

B. Channel Estimation

Given the received signal model in (19), the radar channel, containing information about all reflectors in the considered scene, can be estimated at the ISAC receiver, which is assumed to be co-located with the transmitter (see Fig. 1).

First of all, $\mathbf{R}$ undergoes an order N DFT; this produces

$$\mathbf{Y} = \mathbf{R}\,\boldsymbol{\Xi}_N = \sum_{l=0}^{L-1} (\mathbf{X} \odot \mathbf{H}_l)\, \boldsymbol{\Xi}_N^H\, \mathbf{D}_l\, \boldsymbol{\Xi}_N + \mathbf{W}\,\boldsymbol{\Xi}_N. \tag{20}$$

The last result can be simplified if we assume that all the Doppler frequencies $\{\nu_l\}$ do not exceed the SEFDM subcarrier spacing, i.e., that $|\nu_l| < \beta\Delta_f$ for any l; this is equivalent to assuming a limited channel variations, as usually done in the study of OFDM-based sensing. In fact, under the last assumption, $\boldsymbol{\Xi}_N^H \mathbf{D}_l \boldsymbol{\Xi}_N \cong \mathbf{I}_N$ for any l, so that (20) can be rewritten as

$$\mathbf{Y} \cong \mathbf{X} \odot \mathbf{H} + \bar{\mathbf{W}}, \tag{21}$$

where

$$\mathbf{H} \triangleq \sum_{l=0}^{L-1} \mathbf{H}_l \tag{22}$$

represents the overall channel matrix and $\bar{\mathbf{W}} \triangleq \mathbf{W}\boldsymbol{\Xi}_N$. Since the receiver is assumed to be co-located with the transmitter, the data symbol matrix $\mathbf{X}$ (16) is known; consequently, an estimate of $\mathbf{H}$ (22) can be obtained from (21) by evaluating[4]

$$\hat{\mathbf{H}} = \mathbf{Y} \oslash \mathbf{X} \cong \mathbf{H} + \breve{\mathbf{W}}, \tag{23}$$

where $\breve{\mathbf{W}} \triangleq \bar{\mathbf{W}} \oslash \mathbf{X}$ is an $M \times N$ noise matrix.

As it can be easily inferred from (17) and (22), the elements of $\hat{\mathbf{H}}$ (23) form a 2D sequence consisting of L distinct complex tones superimposed with noise. The parameters of each tone

[3]The dependence of the matrix $\mathbf{H}_l$ on the target parameters $(\breve{a}_l, f_{\tau_l}, f_{\nu_l})$ is not explicitly shown in (15) and in the following to ease notation.

[4]A conceptually similar symbol division approach has been proposed in the context of OFDM-based radar systems (e.g., see [15, Eq. (5)]).

provide information about the range, the radial speed and the radar cross section of a specific point target. Consequently, radar sensing can be performed by applying an algorithm for 2D harmonic retrieval to the matrix $\bar{\mathbf{H}}$ (23), that collects the available set of noisy measurements.

It is worth noting that, after the DFT operation, in (20), the transformed noise matrix $\bar{\mathbf{W}}$ still contains i.i.d. Gaussian noise samples due to the unitary nature of the DFT operator. However, when computing the element-wise division in (23), the entries of $\bar{\mathbf{W}}$ are divided by the known data symbols in $\mathbf{X}$, which belong to a modulation constellation (e.g., *phase-shift keying*, PSK, or *quadrature amplitude modulation*, QAM). As a consequence, the noise samples in the resulting matrix $\breve{\mathbf{W}}$ are no longer i.i.d. and their variances depend on the modulus of the corresponding entries in $\mathbf{X}$. On the one hand, when a QAM modulation is used, the amplitude of the symbols varies, leading to a non-uniform noise power across the matrix; this is exacerbated in the case of SEFDM due to the intentional ICI. This implies that the classical ML estimation metric, which typically assumes i.i.d. noise, becomes suboptimal in both OFDM and SEFDM. On the other hand, when a constant-modulus constellation such as PSK is employed, all the elements of $\mathbf{X}$ have the same magnitude, and the samples of $\breve{\mathbf{W}}$ retain a uniform variance, making the AWGN assumption valid and preserving the optimality of the classical ML metric when $\beta = 1$ (i.e., in the OFDM case) only. A novel technique for accomplishing this last task is described in the following section, under the assumption of i.i.d. noise samples affecting the channel estimates (23).

It is worth pointing out that the adoption of a CP in SEFDM, similarly to OFDM, has an important impact on both SE and estimation accuracy. In fact, on the one hand, the CP reduces the overall SE. On the other hand, however, it makes the adoption of the Fourier-based representation (8) possible and eliminates ISI, thus allowing the straightforward channel estimation procedure[5] expressed by (23). Conversely, if the CP was not employed, (8) would not hold and adjacent blocks would interfere, so that the simple estimation method in (23) would no longer be applicable; therefore, substantially more complicated estimation methods would be required.

III. Approximate Maximum Likelihood Estimation of Channel Parameters

This section is organized into two parts. In the former, we develop a novel algorithm for estimating the set $\mathcal{S}_{\mathrm{H}} \triangleq \{(\breve{a}_l, f_{\nu_l}, f_{\tau_l}); l = 0, 1, \ldots, L-1\}$, that collects the parameters of the L 2D complex exponentials contributing to the channel matrix $\mathbf{H}$ (22). In the second part, we analyze the computational complexity of the proposed method.

A. Derivation of the Proposed Algorithm

To begin, we rewrite the model (23) in vector form as

$$\hat{\mathbf{h}} \triangleq \mathrm{vec}(\hat{\mathbf{H}}) = \mathbf{h} + \breve{\mathbf{w}}, \tag{24}$$

where $\mathbf{h} \triangleq \mathrm{vec}(\mathbf{H})$ and $\breve{\mathbf{w}} \triangleq \mathrm{vec}(\breve{\mathbf{W}})$ are (MN)-dimensional column vectors. Based on (17) and (22), the vector $\mathbf{h}$ can be expressed as

$$\mathbf{h}(\mathbf{a}, \mathbf{f}_\tau, \mathbf{f}_\nu) = \mathbf{B}(\mathbf{f}_\tau, \mathbf{f}_\nu)\, \mathbf{a}; \tag{25}$$

[5]Note this procedure makes an accurate recovery of the channel matrix $\mathbf{H}$ (22) possible in the absence of channel noise.

here,

$$\mathbf{B}(\mathbf{f}_\tau, \mathbf{f}_\nu) \triangleq \mathbf{C}_N^*(\mathbf{f}_\tau) \circledast \mathbf{C}_M(\mathbf{f}_\nu) \tag{26}$$

is an $(MN) \times L$ matrix,

$$\mathbf{C}_p(\mathbf{f}) \triangleq [\bar{\mathbf{b}}_0(\mathbf{f}), \bar{\mathbf{b}}_1(\mathbf{f}), \ldots, \bar{\mathbf{b}}_{p-1}(\mathbf{f})]^T \tag{27}$$

is a $p \times L$ matrix for any positive integer p,

$$\bar{\mathbf{b}}_x(\mathbf{f}) \triangleq [\bar{b}_x(f_0), \bar{b}_x(f_1), \ldots, \bar{b}_x(f_{L-1})]^T \tag{28}$$

is an L-dimensional column vector and $\bar{b}_x(f_l) \triangleq \exp(j2\pi x f_l)$ for any l. Moreover,

$$\mathbf{a} \triangleq [\breve{a}_0, \breve{a}_1, \ldots, \breve{a}_{L-1}]^T, \tag{29}$$

$$\mathbf{f}_\tau \triangleq [f_{\tau_0}, f_{\tau_1}, \ldots, f_{\tau_{L-1}}]^T \tag{30}$$

and

$$\mathbf{f}_\nu \triangleq [f_{\nu_0}, f_{\nu_1}, \ldots, f_{\nu_{L-1}}]^T \tag{31}$$

are the L-dimensional column vectors collecting the complex gains, the normalized delays and normalized Doppler frequencies, respectively, that characterize the considered channel. Given the estimate $\hat{\mathbf{h}}$ (24) of $\mathbf{h}$, our goal is to determine its inner structure by estimating L and $\mathcal{S}_{\mathrm{H}}$; this is equivalent to solving the problem of target detection and estimation in a SEFDM-based radar system, in which the lth target is modeled as a point target with parameters $(\breve{a}_l, f_{\tau_l}, f_{\nu_l})$.

For this reason, if L is known, the problem of target estimation can be formulated as a ML estimation problem. Specifically, given the observation vector $\hat{\mathbf{h}}$, we aim to estimate the unknown target parameters $(\mathbf{a}, \mathbf{f}_\tau, \mathbf{f}_\nu)$, under the assumption that the noise vector $\breve{\mathbf{w}}$ in (24) is a realization of a zero-mean circularly symmetric complex Gaussian random vector with independent entries, having zero mean and variance σ_{w}^2. Given this assumption, the conditional *probability density function* (PDF) of $\hat{\mathbf{h}}$, conditioned on the trial values $(\tilde{\mathbf{a}}, \tilde{\mathbf{f}}_\tau, \tilde{\mathbf{f}}_\nu)$ of the mentioned unknown parameters, is

$$p(\hat{\mathbf{h}}|\tilde{\mathbf{a}}, \tilde{\mathbf{f}}_\tau, \tilde{\mathbf{f}}_\nu) = \frac{1}{(\pi\sigma_{\mathrm{w}}^2)^{MN}} \exp\left(-\frac{1}{\sigma_{\mathrm{w}}^2} \left\|\hat{\mathbf{h}} - \mathbf{h}(\tilde{\mathbf{a}}, \tilde{\mathbf{f}}_\tau, \tilde{\mathbf{f}}_\nu)\right\|^2\right). \tag{32}$$

The ML estimate $(\hat{\mathbf{a}}, \hat{\mathbf{f}}_\tau, \hat{\mathbf{f}}_\nu)$ of $(\mathbf{a}, \mathbf{f}_\tau, \mathbf{f}_\nu)$ is therefore achieved by maximizing the likelihood function (32), as

$$(\hat{\mathbf{a}}, \hat{\mathbf{f}}_\tau, \hat{\mathbf{f}}_\nu) \triangleq \arg \max_{\tilde{\mathbf{a}}, \tilde{\mathbf{f}}_\tau, \tilde{\mathbf{f}}_\nu} p(\hat{\mathbf{h}}, |, \tilde{\mathbf{a}}, \tilde{\mathbf{f}}_\tau, \tilde{\mathbf{f}}_\nu). \tag{33}$$

Equivalently, since the exponential function, in (32), is monotonically increasing, the ML estimation problem can be reformulated as the minimization of the squared error appearing in the same function. This easily leads to

$$(\hat{\mathbf{a}}, \hat{\mathbf{f}}_\tau, \hat{\mathbf{f}}_\nu) \triangleq \arg \min_{\tilde{\mathbf{a}}, \tilde{\mathbf{f}}_\tau, \tilde{\mathbf{f}}_\nu} \mathcal{L}(\hat{\mathbf{h}}|\, \tilde{\mathbf{a}}, \tilde{\mathbf{f}}_\tau, \tilde{\mathbf{f}}_\nu), \tag{34}$$

where

$$\mathcal{L}(\hat{\mathbf{h}}|\, \tilde{\mathbf{a}}, \tilde{\mathbf{f}}_\tau, \tilde{\mathbf{f}}_\nu) \triangleq \mathrm{Tr}\left\{\left(\hat{\mathbf{h}} - \mathbf{h}(\tilde{\mathbf{a}}, \tilde{\mathbf{f}}_\tau, \tilde{\mathbf{f}}_\nu)\right)\left(\hat{\mathbf{h}} - \mathbf{h}(\tilde{\mathbf{a}}, \tilde{\mathbf{f}}_\tau, \tilde{\mathbf{f}}_\nu)\right)^H\right\} \tag{35}$$

is a *log-likelihood* (LL) cost function for the optimization problem (34). Given $\tilde{\mathbf{f}}_\tau$ and $\tilde{\mathbf{f}}_\nu$, the minimum of $\mathcal{L}(\hat{\mathbf{h}}|\, \tilde{\mathbf{a}}, \tilde{\mathbf{f}}_\tau, \tilde{\mathbf{f}}_\nu)$ with respect to $\tilde{\mathbf{a}}$ is obtained by 1) substituting the expression of $\mathbf{h}(\cdot, \cdot, \cdot)$ (25) in the RHS of (35), 2) taking the derivative

of the resulting expression with respect to $\tilde{\mathbf{a}}$, 3) setting it to zero and 4) solving for $\hat{\mathbf{a}} = \tilde{\mathbf{a}}$; this results in

$$\hat{\mathbf{a}} = \mathbf{B}^{\dagger}(\tilde{\mathbf{f}}_{\tau}, \tilde{\mathbf{f}}_{\nu})\,\hat{\mathbf{h}}. \tag{36}$$

Unfortunately, given $\tilde{\mathbf{a}} = \hat{\mathbf{a}}$, the minimization of (35) with respect to $\tilde{\mathbf{f}}_{\tau}$ and $\tilde{\mathbf{f}}_{\nu}$ does not lead to a closed-form solution. However, if a coarse estimate of both $\tilde{\mathbf{f}}_{\tau}$ and $\tilde{\mathbf{f}}_{\nu}$ is available, a Newton-based method can be adopted to solve the optimization problem in (34). This approach requires evaluating the gradient vector and the Hessian matrix of $\mathcal{L}$ (35) with respect to the vector $\tilde{\mathbf{f}} \triangleq [\tilde{\mathbf{f}}_{\tau}^{T}\ \tilde{\mathbf{f}}_{\nu}^{T}]^{T}$.

Proposition 1: The gradient vector and the Hessian matrix of $\mathcal{L}$ can be expressed as[6]

$$\nabla_{\mathcal{L}}(\tilde{\mathbf{a}}, \tilde{\mathbf{f}}) = -2\left[\Re\left\{\tilde{\mathbf{a}}^{*} \odot \dot{\mathbf{B}}_{\tilde{\mathbf{f}}_{\tau}}^{H}(\hat{\mathbf{h}} - \mathbf{B}\tilde{\mathbf{a}})\right\}^{T}, \Re\left\{\tilde{\mathbf{a}}^{*} \odot \dot{\mathbf{B}}_{\tilde{\mathbf{f}}_{\nu}}^{H}(\hat{\mathbf{h}} - \mathbf{B}\tilde{\mathbf{a}})\right\}^{T}\right]^{T}, \tag{37}$$

and as

$$\ddot{\mathbf{H}}_{\mathcal{L}}(\tilde{\mathbf{a}}, \tilde{\mathbf{f}}) \triangleq \begin{bmatrix} \mathbf{T}_{\tilde{\mathbf{f}}_{\tau}, \tilde{\mathbf{f}}_{\tau}} & \mathbf{U}_{\tilde{\mathbf{f}}_{\tau}, \tilde{\mathbf{f}}_{\nu}} \\ \mathbf{U}_{\tilde{\mathbf{f}}_{\tau}, \tilde{\mathbf{f}}_{\nu}} & \mathbf{V}_{\tilde{\mathbf{f}}_{\nu}, \tilde{\mathbf{f}}_{\nu}} \end{bmatrix}, \tag{38}$$

respectively; here,[7]

$$\mathbf{T}_{\tilde{\mathbf{f}}_{\tau}, \tilde{\mathbf{f}}_{\tau}} \triangleq \left[\frac{\partial^{2}\mathcal{L}}{\partial \tilde{f}_{\tau_l} \partial \tilde{f}_{\tau_{l'}}}\right] = 2\Re\left\{(\tilde{\mathbf{a}}\,\tilde{\mathbf{a}}^{H}) \odot \left(\dot{\mathbf{B}}_{\tilde{\mathbf{f}}_{\tau}}^{H} \dot{\mathbf{B}}_{\tilde{\mathbf{f}}_{\tau}}^{*}\right) - \left(\tilde{\mathbf{a}}^{*}\left(\hat{\mathbf{h}} - \mathbf{B}\tilde{\mathbf{a}}\right)^{H} \ddot{\mathbf{B}}_{\tilde{\mathbf{f}}_{\tau}, \tilde{\mathbf{f}}_{\tau}}\right)\right\}, \tag{39}$$

$$\mathbf{U}_{\tilde{\mathbf{f}}_{\tau}, \tilde{\mathbf{f}}_{\nu}} \triangleq \left[\frac{\partial^{2}\mathcal{L}}{\partial \tilde{f}_{\tau_l} \partial \tilde{f}_{\nu_{l'}}}\right] = 2\Re\left\{(\tilde{\mathbf{a}}\,\tilde{\mathbf{a}}^{H}) \odot \left(\dot{\mathbf{B}}_{\tilde{\mathbf{f}}_{\tau}}^{H} \dot{\mathbf{B}}_{\tilde{\mathbf{f}}_{\nu}}^{*}\right) - \left(\tilde{\mathbf{a}}^{*}\left(\hat{\mathbf{h}} - \mathbf{B}\tilde{\mathbf{a}}\right)^{H} \ddot{\mathbf{B}}_{\tilde{\mathbf{f}}_{\tau}, \tilde{\mathbf{f}}_{\nu}}\right)\right\} \tag{40}$$

and

$$\mathbf{V}_{\tilde{\mathbf{f}}_{\nu}, \tilde{\mathbf{f}}_{\nu}} \triangleq \left[\frac{\partial^{2}\mathcal{L}}{\partial \tilde{f}_{\nu_l} \partial \tilde{f}_{\nu_{l'}}}\right] = 2\Re\left\{(\tilde{\mathbf{a}}\,\tilde{\mathbf{a}}^{H}) \odot \left(\dot{\mathbf{B}}_{\tilde{\mathbf{f}}_{\nu}}^{H} \dot{\mathbf{B}}_{\tilde{\mathbf{f}}_{\nu}}^{*}\right) - \left(\tilde{\mathbf{a}}^{*}\left(\hat{\mathbf{h}} - \mathbf{B}\tilde{\mathbf{a}}\right)^{H} \ddot{\mathbf{B}}_{\tilde{\mathbf{f}}_{\nu}, \tilde{\mathbf{f}}_{\nu}}\right)\right\} \tag{41}$$

are $L \times L$ matrices. Moreover, $\dot{\mathbf{B}}_{\tilde{\mathbf{f}}_{x}}$ is an $(MN) \times L$ matrix, whose lth column contains the partial derivative of the lth column of $\mathbf{B}$ (see (26) with $(\mathbf{f}_{\tau}, \mathbf{f}_{\nu}) = (\tilde{\mathbf{f}}_{\tau}, \tilde{\mathbf{f}}_{\nu})$), evaluated with respect to $\tilde{f}_{x}$. Similarly, $\ddot{\mathbf{B}}_{\tilde{\mathbf{f}}_{x}, \tilde{\mathbf{f}}_{y}}$ is a $(MN) \times L$ matrix, whose lth column contains the second-order derivative of the lth column of $\mathbf{B}$ (26) evaluated with respect to $\tilde{f}_{x}$ and $\tilde{f}_{y}$. Note that, thanks to the linearity property of the derivative, the equality $\ddot{\mathbf{B}}_{\tilde{\mathbf{f}}_{x}, \tilde{\mathbf{f}}_{y}} = \ddot{\mathbf{B}}_{\tilde{\mathbf{f}}_{y}, \tilde{\mathbf{f}}_{x}}$ holds.

Proof: The results illustrated in this proposition are proven in Appendix A □.

Given the previous results, an iterative procedure for estimating the parameters $\mathbf{a}$, $\mathbf{f}_{\tau}$ and $\mathbf{f}_{\nu}$ can be formulated as follows:

1) *Initialization*–The initial values $\hat{\mathbf{a}}^{(0)}$, $\hat{\mathbf{f}}_{\tau}^{(0)}$ and $\hat{\mathbf{f}}_{\nu}^{(0)}$ are obtained through the 2D *periodogram method*,[8] that also generates an estimate $\hat{L}$ of L. This method is based on a peak search on the 2D spectrum of $\hat{\mathbf{H}}$ (23) and produces $\hat{L}$ couples of 2D frequencies, associated with the delay and Doppler of $\hat{L}$ targets. Here, we assume that all point targets are sufficiently spaced along the delay and Doppler dimensions, so that the peaks appearing in the 2D spectrum evaluated for the received signal can be easily identified without ambiguity. Under this condition,[9] an estimate[10] $\hat{L}$ of L can be obtained by adopting a proper detection threshold ϵ_{init} in the evaluation of the local maxima of the above mentioned 2D spectrum. Note that this threshold is typically selected in a way to minimize the detection of false (i.e., ghost) spectral components; for instance, the *generalized likelihood ratio test*, GLRT, can be been employed [18, Par. 4.6.1]). Then, the $\hat{L}$ estimated 2D frequencies are organized in the $(2\hat{L})$-dimensional vector $\hat{\mathbf{f}}^{(0)} = [(\hat{\mathbf{f}}_{\tau}^{(0)})^{T}(\hat{\mathbf{f}}_{\nu}^{(0)})^{T}]^{T}$. Finally, the iteration index i is set to 1.

2) *Refinement procedure*–An iterative procedure, consisting of the following three steps, is executed.

2a) *Complex amplitude update*–The new complex amplitude vector $\hat{\mathbf{a}}^{(i)}$ is computed through (36) with $(\tilde{\mathbf{f}}_{\tau}, \tilde{\mathbf{f}}_{\nu}) = (\hat{\mathbf{f}}_{\tau}^{(i-1)}, \hat{\mathbf{f}}_{\nu}^{(i-1)})$, where $\hat{\mathbf{f}}_{\tau}^{(i-1)}$ and $\hat{\mathbf{f}}_{\nu}^{(i-1)}$ denote the estimates of $\mathbf{f}_{\tau}$ and $\mathbf{f}_{\nu}$, respectively, available at the end of the $(i-1)$th iteration.

2b) *Frequency update*–The new estimate

$$\hat{\mathbf{f}}^{(i)} = \hat{\mathbf{f}}^{(i-1)} - \mu\,\ddot{\mathbf{H}}_{\mathcal{L}}^{-1}\left(\hat{\mathbf{a}}^{(i)}, \hat{\mathbf{f}}^{(i-1)}\right)\nabla_{\mathcal{L}}\left(\hat{\mathbf{a}}^{(i)}, \hat{\mathbf{f}}^{(i-1)}\right), \tag{42}$$

is computed; here, $\hat{\mathbf{f}}^{(i)} = [(\hat{\mathbf{f}}_{\tau}^{(i)})^{T}(\hat{\mathbf{f}}_{\nu}^{(i)})^{T}]^{T}$ and μ is a real positive parameter representing the step size of the proposed method. In our simulations, the step size μ has been set to one.[11]

2c) *Convergence test*–The quantity

$$\Delta\mathcal{L}^{(i)} \triangleq \left|\mathcal{L}\left(\hat{\mathbf{h}}\middle|\,\hat{\mathbf{a}}^{(i)}, \hat{\mathbf{f}}_{\tau}^{(i)}, \hat{\mathbf{f}}_{\nu}^{(i)}\right) - \mathcal{L}\left(\hat{\mathbf{h}}\middle|\,\hat{\mathbf{a}}^{(i-1)}, \hat{\mathbf{f}}_{\tau}^{(i-1)}, \hat{\mathbf{f}}_{\nu}^{(i-1)}\right)\right| \tag{43}$$

is evaluated (see (35)). Then, this last value is compared with a proper threshold[12] ϵ_{it}. If $\Delta\mathcal{L}^{(i)} > \epsilon_{\text{it}}$, the iteration index i is increased by one and, if $i < N_{\text{it}}$, steps **2a)**-**2b)**-**2c)** are repeated. Otherwise, the algorithm stops, and the quantities $\hat{\mathbf{a}}^{(i)}$, $\hat{\mathbf{f}}_{\tau}^{(i)}$ and $\hat{\mathbf{f}}_{\nu}^{(i)}$ are taken as output.

The NMCR algorithm is summarized in Algorithm 1.

B. Computational Complexity Analysis

It is not difficult to show that the overall computational cost of a single iteration of the refinement procedure of the NMCR algorithm in the presence of L targets can be expressed as $\mathcal{O}((L + L^{2})\,M\,N)$.

The proposed procedure requires an initial estimate of the frequencies $\mathbf{f}_{\tau}$ and $\mathbf{f}_{\nu}$. If the 2D-FFT method is used to

[6] The dependence of the matrix $\mathbf{B}$ (26) on the variables $(\tilde{\mathbf{f}}_{\tau}, \tilde{\mathbf{f}}_{\nu})$ is not explicitly shown in the following to ease reading.

[7] Note that the dependence of the matrices $\mathbf{T}_{\tilde{\mathbf{f}}_{\tau}, \tilde{\mathbf{f}}_{\tau}}$, $\mathbf{U}_{\tilde{\mathbf{f}}_{\tau}, \tilde{\mathbf{f}}_{\nu}}$ and $\mathbf{V}_{\tilde{\mathbf{f}}_{\nu}, \tilde{\mathbf{f}}_{\nu}}$ on the variable $\tilde{\mathbf{a}}$ is not explicitly shown to ease notation.

[8] The 2D periodogram method is dubbed 2D-FFT in the following.

[9] If this condition is not met, closely spaced targets may cause partially overlapped peaks, potentially resulting in an incorrect estimate of $\hat{L}$ or a degraded initialization accuracy.

[10] For notational simplicity, in the following we assume $\hat{L} = L$ without loss of generality. It should be noted, however, that the proposed algorithm operates on the available estimate $\hat{L}$, so its applicability is preserved even when $\hat{L} \neq L$.

[11] In principle, one could reduce the value of the step size μ (for instance, it could be halved) if no significant decrease in the value of $\mathcal{L}$ (35) is observed over two consecutive iterations.

[12] The threshold ϵ_{it} can be selected using the same approach adopted for the threshold employed for the initialization step, i.e., ϵ_{init}.

Algorithm 1 Newton-Based Multiple Cisoid Refiner (NMCR)

Input: The vector $\hat{\mathbf{h}}$ (24), the detection threshold $\epsilon_{\rm init}$, the oversampling factors $(L_{\rm D}, L_{\rm r})$ for the 2D-FFT method, the parameter $\epsilon_{\rm it}$, the step size μ and the overall number of iterations $N_{\rm it}$.

1 **Initialization:**
Evaluate the initial estimates $\hat{\mathbf{a}}^{(0)}$, $\hat{\mathbf{f}}_\tau^{(0)}$,$\hat{\mathbf{f}}_\nu^{(0)}$ and $\hat{L}$ by applying the 2D-FFT method to $\hat{\mathbf{h}}$ (24). Then, set the iteration index i to 1.

2 **Refinement:**
2a-*Complex amplitude update*: compute $\hat{\mathbf{a}}^{(i)}$ through (36) with $(\tilde{\mathbf{f}}_\tau, \tilde{\mathbf{f}}_\nu) = (\hat{\mathbf{f}}_\tau^{(i-1)}, \hat{\mathbf{f}}_\nu^{(i-1)})$.
2b-*Frequency update*: Compute $\hat{\mathbf{f}}^{(i)} = [(\hat{\mathbf{f}}_\tau^{(i)})^T (\hat{\mathbf{f}}_\nu^{(i)})^T]^T$ through (42).
2c- *Convergence test*: Evaluate the quantity $\Delta\mathcal{L}^{(i)}$ (43); then, if $\Delta\mathcal{L}^{(i)} > \epsilon_{\rm it}$, the iteration index i is increased by one and, if $i < N_{\rm it}$, steps **2a)-2b)-2c)** are repeated.

Output: The estimates $\hat{\mathbf{a}}^{(i)}$, $\hat{\mathbf{f}}_\tau^{(i)}$, $\hat{\mathbf{f}}_\nu^{(i)}$ and $\hat{L}$ of $\mathbf{a}$, $\mathbf{f}_\tau$,$\mathbf{f}_\nu$ and L, respectively.

compute this estimate, the complexity of the initialization is $\mathcal{O}(N_{\text{2D-FFT}})$, with (e.g., see [16, Sec. III-A.1,Eq. (26)])

$$N_{\text{2D-FFT}} = M_0 N_0 \log_2(M_0 N_0) + M_0 N_0 + L \log_2(L); \quad (44)$$

here, $M_0 \triangleq M L_{\rm D}$, $N_0 \triangleq N L_{\rm r}$, whereas $L_{\rm D}$ and $L_{\rm r}$ are the so-called *oversampling factors* that are selected for the *discrete symplectic Fourier transform* (DSFT) operation[13] executed along the rows and columns of $\hat{\mathbf{H}}$ (23), respectively.

Therefore, the overall computational cost of the NMCR algorithm is $\mathcal{O}(N_{\rm NMCR})$, with

$$N_{\rm NMCR} \triangleq N_{\text{2D-FFT}} + N_{\rm it}(L + L^2)\, M\, N. \quad (45)$$

IV. Numerical Results

In this section, we assess the accuracy of the NMCR algorithm in six different scenarios and we compare it with that achieved by the following four algorithms: 1) the 2D-FFT method [9]; 2) a refinement procedure based on interpolation of the 2D periodogram [19, Sec. IV-A]; 3) the approximate ML method, based on *alternating projections* (APs), recently proposed in [14]; 4) the *expectation maximization* (EM) algorithm [14]. In the following, the last three methods are denoted 2D-FFTi, AP-ML and EM, respectively. Note that such methods have originally been developed in the context of OFDM, but can be easily adapted to SEFDM.

The characteristics of the considered scenarios can be summarized as follows (the ith scenario is denoted **S**i in the following):

S1) This is characterized by a single target (i.e., $L = 1$) having unitary amplitude A_0, and whose range R_0 and velocity v_0 are random variables uniformly distributed in $[R_{\min}, R_{\max}]$ and $[v_{\min}, v_{\max}]$, respectively; in our simulations, $[R_{\min}, R_{\max}] = [5, 45]$ m and $[v_{\min}, v_{\max}] = [5, 50]$ m/s have been selected.

S2) This is characterized by $L = 2$ targets. The parameters (A_0, R_0, v_0) of the first target are generated in the same way as those given for **S1**, whereas those of the second target, namely (A_1, R_1, v_1) have been selected in a way that $A_1 = 0.8 + 0.2\,\bar{\alpha}\,A_0$, $R_1 = R_0 + \bar{R}\,R_{\rm bin}$ and $v_1 = v_0 + \bar{v}\,v_{\rm bin}$, respectively; here, $\bar{\alpha}$ is a random variable uniformly distributed over the interval $[0, 1]$, $\bar{R}$ and $\bar{v}$ represent the normalized spacing in range and Doppler, respectively (both have been set to 3 in our simulations referring to **S2**), and

$$R_{\rm bin} \triangleq \frac{c}{2N\beta\Delta_f}, \quad v_{\rm bin} \triangleq \frac{c\,\beta}{2M f_{\rm c} T_{\rm s}} \quad (46)$$

denote the range and velocity resolutions, respectively, for the considered SEFDM-based radar system.

S3) This is characterized by $L = 5$ targets. The parameters (A_0, R_0, v_0) of the first target have been generated in the same way as **S1**; however, $[R_{\min}, R_{\max}] = [10, 35]$ m and $[v_{\min}, v_{\max}] = [30, 50]$ m/s have been chosen in the generation of R_0 and v_0. Moreover, the following choices have been made for the lth target (with $l = 1, 2, 3, 4$): 1) $R_l = R_0 + 2l(\bar{\alpha} - 0.5)R_{\rm bin}$; 2) $v_l = v_0$; 3) A_l, being generated according to *Swerling*-3 model (e.g., see [20, Eq. (7)]), follows a *chi-square* distribution with a mean value equal to A_0.

S4) This is characterized by $L = 3$ targets. The parameters of the first target have been generated in the same way as **S1**. Moreover, the following choices have been made for the lth target (with $l = 1, 2$): 1) $A_l = A_0 = 1$; 2) the target ranges and velocities have been generated in the same way as **S2**, but $\bar{R} = 1.25$ and $\bar{v} = 1.75$ have been selected.

S5) This is characterized by a variable number of targets $L \in \{1, 2, \ldots, 8\}$. The parameters of the first target have been generated in the same way as **S3**, whereas those of the lth target (with $l = 1, 2, \ldots, L-1$) have been produced in the same way as **S2**, but $\bar{R} = \bar{v} = 1$ have been chosen.

S6) This scenario is characterized by a couple of targets (i.e., $L = 2$), whose physical parameters are generated in the same way as **S2**; however, we have that: a) $A_1 = 0.75$, b) $\bar{R} = 2$ and c) $\bar{v} = 2$.

Note that the first three scenarios are characterized by a variable SNR $\in [-20, 10]$ dB,[14] whereas the SNR has been set to -5 dB in both **S4** and **S5**, and to 0 dB in **S6**. The selection of the scenarios described above can be motivated as follows:

1) In **S1**, which is characterized by $L = 1$, target detection and estimation are not affected by the potential spectral leakage originating from the presence of multiple targets.

2) In **S2**, multiple targets are present, but leakage is negligible, the targets being adequately spaced.

3) **S3** is useful to assess the estimation accuracy in the presence of an extended scatterer. In fact, in this case, the targets have a common *centroid* (characterized by the parameters (A_0, R_0, v_0)), share the same velocity and are closely spaced in range. Moreover, the target amplitudes follow a model typically used for extended targets.

4) **S4** and **S5** are characterized by multiple closely spaced targets, each with a fixed SNR. In our analysis, **S4** has been specifically designed to examine the convergence behavior of the proposed NMCR algorithm and compare it with other iterative techniques, namely the AP-ML and EM algorithms. To this end, the dependence of the estimation accuracy on the number of iterations, employed in the frequency refinement

[13] Further details about the 2D-FFT method and its inherent DSFT processing can be found in [16, Sec. III-A.1].

[14] In all the considered scenarios, the impact of the CP on the evaluation of the effective SNR has been considered.

step of each method, has been assessed. Therefore, readers should keep in mind that **S4** provides insight into the stability and robustness of the considered iterative procedures, highlighting how quickly and reliably each algorithm approaches its steady-state performance. In contrast, **S5** has been adopted to assess the dependence of the computational complexity of each method on the number of targets.

5) **S6** has been considered to assess the impact of the compression factor β on sensing performance. A change in this parameter modifies the normalized delay and Doppler frequency of each target, but does not alter the normalized frequency resolutions, which are only determined by the parameters M and N.

In our simulations, we have also considered an additional scenario (denoted as **S0**), whose exclusive scope is the analysis of the detection capability of the GLRT method employed in the initialization step of all the considered algorithms under different SNR conditions, number of targets, and target velocities. In fact, for this scenario, we have assessed the *detection probability* $P_{\rm D}$, i.e., the probability[15] that the estimated number of targets $\hat{L}$ coincides with the true one L. The following assumptions have been made about the targets: 1) $L \in \{1, 3, 5\}$; 2) the parameters of the first target are generated in the same way as **S3**, with velocity values uniformly drawn within $[0.9\ v_{\rm mean}, 1.1\ v_{\rm mean}]$; 3) the parameters of the remaining lth target ($l = 1, 2, \ldots, L-1$) are generated in the same way as **S2**. Moreover, the following two cases have been considered:

Case 1 - The SNR is varied within the interval $[-25, 10]$ dB and the mean target speed $v_{\rm mean} = 50$ km/h is selected. This case allows us to analyze the sensitivity of the GLRT to the noise level for different values of L.

Case 2 - The SNR is set to 0 dB and the mean target speed $v_{\rm mean}$ is varied in the interval $[50, 1700]$ km/h. Results for this case unveil the impact of target velocity on the GLRT detection accuracy.

In all the considered scenarios, the following parameters have been selected for the SEFDM modulation: 1) overall number of subcarriers $N = 64$; 2) overall number of SEFDM symbols per frame $M = 32$; 3) data symbol time $T_{\rm s} = 40$ ns; 4) compression factor $\beta = 0.8$; 5) CP length $N_{\rm cp} = N/4$; 6) roll-off factor for the pulse $p(t)$, $\alpha = 0.15$; 7) carrier frequency $f_{\rm c} = 78$ GHz; 8) (unless differently stated) cardinality of the PSK constellation $M_{\rm c} = 16$. These choices entail that: 1) $\Delta_f = 390.625$ kHz; 2) number of suppressed subcarriers $N_{\rm sc} = 10$ (see comments above [17, Sec. II-A,Eq. (17)]); 3) in the first five scenarios, $R_{\rm bin} = 7.5$ m and $v_{\rm bin} = 18.7$ m/s (see (46)). Note also that, from a communication perspective, the value selected for β in the first five scenarios has allowed us to achieve a good trade-off between SE and data detection complexity; in fact, reducing β improves SE but increases the complexity of data detection due to the stronger impact of intentional ICI [7]. From a sensing perspective, instead, the value of β influences the 2D resolution grid (i.e., the *range-Doppler* map); in fact, selecting a smaller value for this parameter entails a reduction in the spacing between normalized delays and an increase in that between normalized Doppler frequencies. This directly affects the achievable estimation accuracy in multi-target scenarios, as it increases the *Cramér-Rao lower bound*[16] (CRLB) for range estimation, while it lowers that referring to velocity estimation.

In our computer simulations, the estimation accuracy of each algorithm has been assessed by evaluating the *root mean square error* (RMSE) for target range ($\text{RMSE}_{\rm R}$) and velocity ($\text{RMSE}_{\rm v}$). In **S1**, **S2**, **S3** and **S6**, the estimation accuracy has been evaluated for all the considered algorithms. In **S4**, instead, only the iterative techniques (i.e., NMCR, AP-ML and EM algorithms) have been taken into consideration. All performance metrics have been computed as averages over 10^3 Monte Carlo simulations. Finally, in **S5**, the computational complexity, expressed in terms of *mega floating point operations* (MFLOPs), and *execution time*[17] (ET), recorded in seconds, have been assessed; note that these last two metrics refer exclusively to the refinement step of each algorithm, with the exception of the 2D-FFT method, which does not include any refinement procedure.

In all our simulations, the following choices have been made for the considered estimation algorithms:

1) The initial estimates have been generated by the 2D-FFT algorithm; therefore, the same estimates feed the refinement procedure of each of the considered methods.

2) The oversampling factors $L_{\rm D} = 4$ and $L_{\rm r} = 4$ have been chosen for Doppler and range estimation in the 2D-FFT algorithm (so that $M_0 \triangleq ML_{\rm D} = 128$ and $N_0 \triangleq NL_{\rm r} = 256$; see [16, Eqs. (22),(23)], respectively).

3) $N_{F_{\rm D}} = 9$ and $N_{F_{\rm r}} = 9$ have been chosen for the refinement grid in the Doppler and range domains, respectively; this grid is employed by the AP-ML and the EM algorithms (e.g., see [14, Eq. (30)] and [16, Sec. III-C.2 and III-C.4], and related comments).

4) $I_{\rm D} = 7$ and $I_{\rm r} = 7$ have been selected for the interpolation orders[18] adopted in the Doppler and range domains, respectively, by the 2D-FFTi algorithm. The numbers of interpolated points are $\bar{M} = 256$ and $\bar{N} = 256$ for the Doppler and range domains, respectively.

5) Unless stated differently, $N_{\rm it} = 10$ iterations have been executed by the NMCR algorithm for the refinement of the frequency estimates provided by the 2D-FFT method.

6) $N_{\rm it} = 3$ iterations have been executed by both the AP-ML and EM algorithms (unless stated differently) for the refinement of the frequency estimates provided by the 2D-FFT method.

7) A unit value has been assigned to all the mixing coefficients $\{\beta_l^{(i)}; l = 0, 1, \ldots, L-1\}$ of the EM algorithm (see [16, Eq. (91)] and related comments).

The values selected for the considered estimation algorithms in our simulations are summarized in Table I.

The overall computational complexity orders of the frequency refinement algorithms considered in our simulations are listed in Table II. Note that the computational complexities of the EM and AP-ML algorithms are provided in [16, Table 2], whereas that related to the 2D-FFTi algorithm can be found in [19, Eqs. (137)-(138)].

[15]The GLRT threshold $\epsilon_{\rm init}$ has been selected in a way to ensure a constant false alarm probability $P_{\rm fa} = 10^{-3}$.

[16]Some guidelines about the evaluation of this performance bound can be found in Appendix B.

[17]The ET has been measured on a personal computer equipped with an i9 processor and 32 GB of RAM.

[18]In our simulations, the `interp2` function, with 2D *spline* interpolation, of Matlab R2024a has been always employed.

TABLE I

VALUES OF THE PARAMETERS SELECTED IN OUR SIMULATIONS

Parameter	**Value / Description**
Initial estimate source	2D-FFT output (common to all algorithms)
2D-FFT oversampling factors	$L_{\mathrm{D}} = 4$, $L_{\mathrm{r}} = 4$
Refinement grid size (AP-ML, EM)	$N_{F_{\mathrm{D}}} = 9$, $N_{F_{\mathrm{r}}} = 9$
Interpolation orders (2D-FFTi)	$I_{\mathrm{D}} = 7$, $I_{\mathrm{r}} = 7$
Interpolated grid sizes (2D-FFTi)	$\bar{M} = 256$, $\bar{N} = 256$
Step size & number of iterations (NMCR)	$\mu = 1$, $N_{\mathrm{it}} = 10$ (unless differently stated)
Number of iterations (AP-ML, EM)	$N_{\mathrm{it}} = 3$ (unless differently stated)
EM mixing coefficients	$\beta_l^{(i)} = 1, \forall l \in \{0, 1, ..., \hat{L} - 1\}$

TABLE II

COMPUTATIONAL COMPLEXITY ORDER OF FREQUENCY REFINEMENT ALGORITHMS

Algorithm	NMCR	2D-FFTi	AP-ML	EM
Initialization $\mathcal{O}(\cdot)$	$N_{\text{2D-FFT}}$ (44)	$N_{\text{2D-FFT}}$ (44)	$N_{\text{2D-FFT}}$ (44)	$N_{\text{2D-FFT}}$ (44)
Refinement $\mathcal{O}(\cdot)$	$N_{\mathrm{it}}(L + L^2)\, M\, N$	$2(I_{\mathrm{D}}\, I_{\mathrm{r}} + \bar{M}\, \bar{N}) + L\, \bar{M}\, \bar{N}$	$8N_{\mathrm{it}}(N_{F_{\mathrm{D}}} + N_{F_{\mathrm{r}}})(L^2 + L)(MN)^2$	$LN_{\mathrm{it}}\, M\, N(4N_{F_{\mathrm{D}}} N_{F_{\mathrm{r}}} + L)$

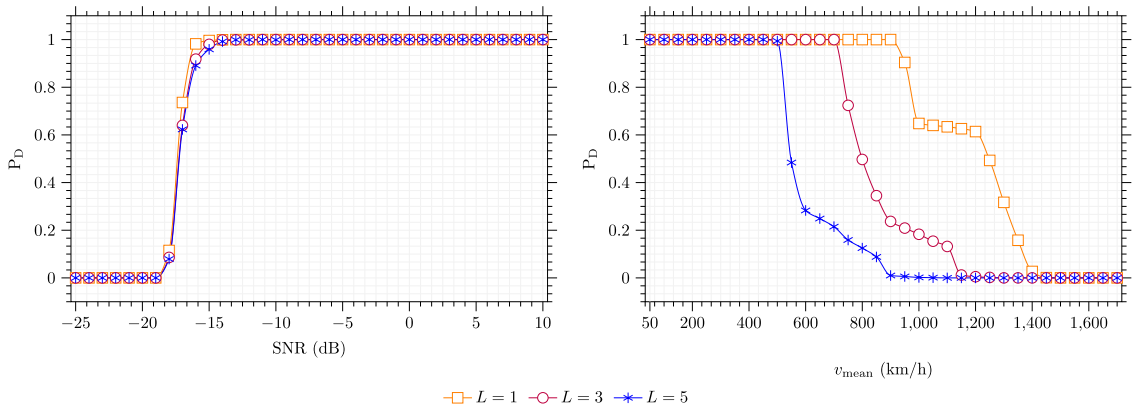

Fig. 3. Detection probability, P_{D}, achieved by the GLRT method in **S0** for: 1) SNR $\in [-25, 10]$ dB and $v_{\mathrm{mean}} = 50$ km/h (left figure) and 2) SNR = 0 dB and $v_{\mathrm{mean}} \in [50, 1700]$ km/h (right figure). In both cases, $L \in \{1, 3, 5\}$ has been assumed.

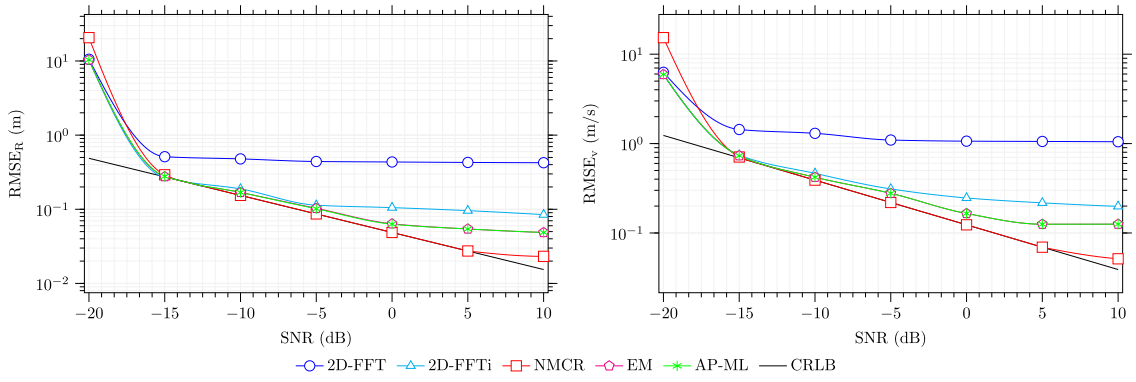

Fig. 4. Root mean square error performance achieved by 2D-FFT, 2D-FFTi, NMCR, EM and AP-ML algorithms, in range (left figure) and velocity estimation (right figure); **S1** and a 16-PSK constellation are assumed. The CRLBs for range and velocity are also shown as references.

Some numerical results referring to **S0** are illustrated in Fig. 3. These results show that: 1) the detection probability increases with SNR and approaches unity above approximately -13 dB, with only a slight degradation as the number of targets L grows; 2) at SNR $= 0$ dB, the detection probability closely approaches unity up to about 1000, 800, and 600 km/h

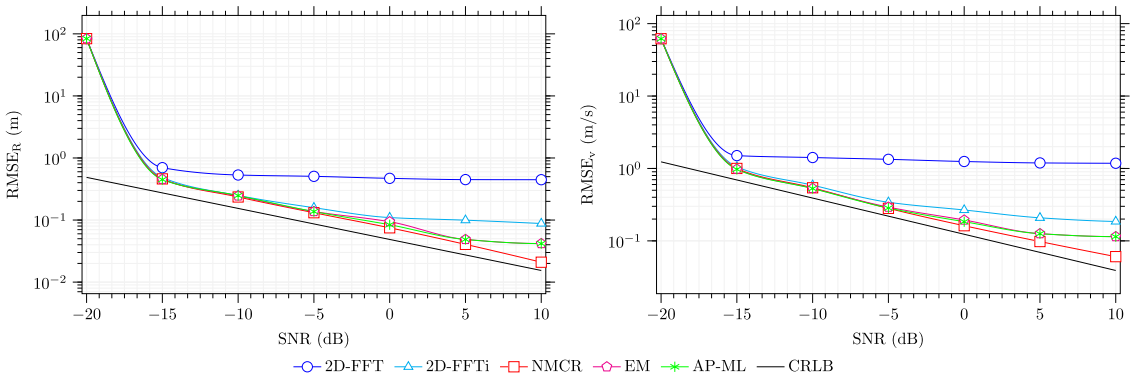

Fig. 5. Root mean square error performance achieved by 2D-FFT, 2D-FFTi, NMCR, EM and AP-ML algorithms, in range (left figure) and velocity estimation (right figure); **S1** and a 16-QAM constellation are assumed. The CRLBs for range and velocity are also shown as references.

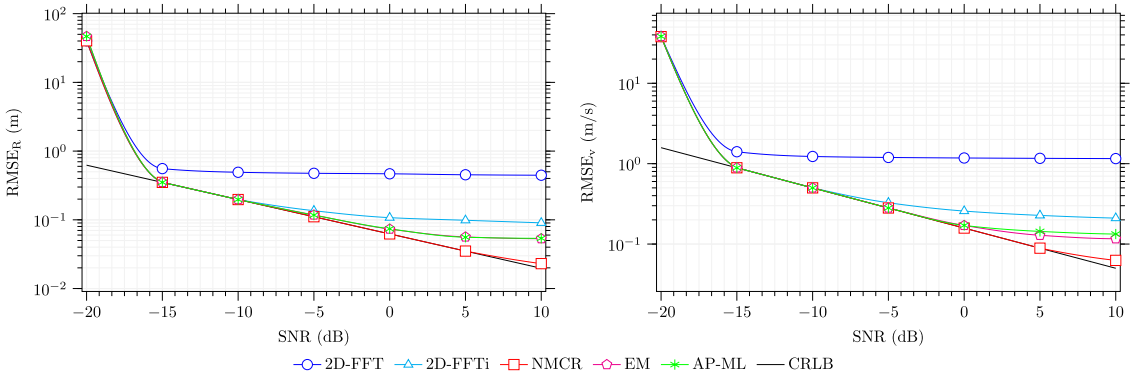

Fig. 6. Root mean square error performance achieved by 2D-FFT, 2D-FFTi, NMCR, EM and AP-ML algorithms, in range (left figure) and velocity estimation (right figure) in **S2**. The CRLBs for range and velocity are also shown as references.

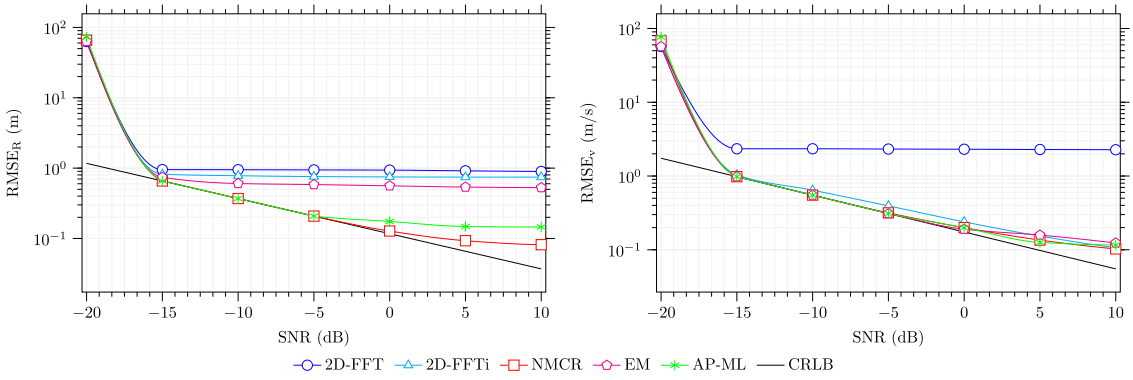

Fig. 7. Root mean square error performance achieved by 2D-FFT, 2D-FFTi, NMCR, EM and AP-ML algorithms, in range (left figure) and velocity estimation (right figure) in **S3**. The CRLBs for range and velocity are also shown as references.

for $L = 1$, $L = 3$, and $L = 5$, respectively. Beyond these values, P_D decreases as the mean target velocity increases, with a more pronounced degradation as L gets larger. These results highlight the inherent limitations of the SEFDM-radar architecture under high-mobility conditions, as it also happens in OFDM-based systems because of the stronger impact of ICI.

Some numerical results referring to **S1** are provided in Figs. 4 and 5, where the RMSE$_R$ and the RMSE$_v$ characterizing all the considered algorithms are shown; note that Figs. 4 and 5 refer to the use of different constellations and, in particular, to 16-PSK and 16-QAM, respectively. Based on the results illustrated in Fig. 4, the following observations can be made:

1) The 2D-FFTi, NMCR, AP-ML and EM algorithms are substantially more accurate than the 2D-FFT, whose accuracy is limited by the FFT bin resolutions in range and Doppler. In fact, this algorithm does not include any frequency refinement procedure and can only leverage oversampling in the

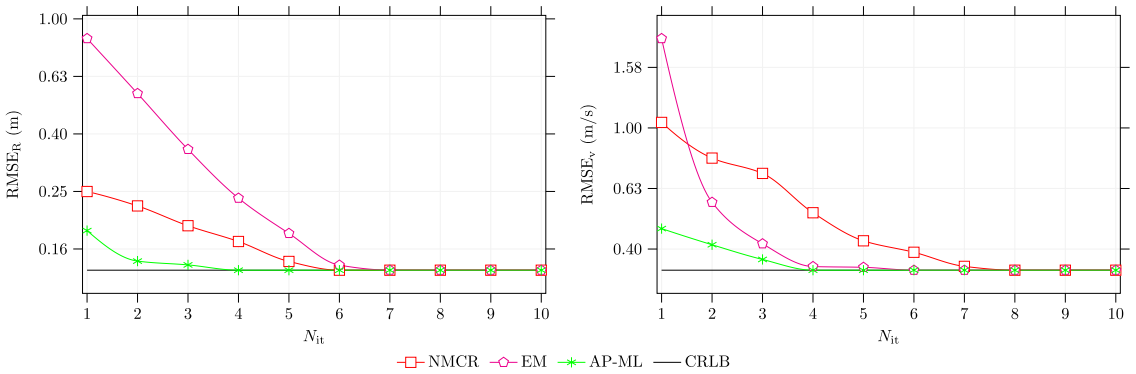

Fig. 8. Root mean square error performance achieved by NMCR, EM and AP-ML algorithms, in range (left figure) and velocity estimation (right figure) in **S4**. An SNR $= -5$ dB has been considered and the CRLBs for range and velocity are also shown as references.

evaluation of the 2D spectrum. This limits its complexity at the price of worse estimation.

2) The interpolation adopted by the 2D-FFTi improves the 2D-FFT estimates by approximately a factor of 4 for an SNR $\in [-5, 10]$ dB with a limited increase in the computational complexity (this is due to the interpolation of a few adjacent points in the 2D spectrum for each detected target).

3) The NMCR algorithm outperforms all the other techniques in terms of both RMSE$_R$ and RMSE$_v$. At 5 dB, it approximately achieves a 50% greater accuracy than both the EM and AP-ML algorithms in estimating range and velocity. Its trend follows closely that of the CRLB for an SNR not higher than 5 dB in both range and velocity estimation. Further numerical results have evidenced that the RMSE floor developing for a large SNR can be reduced by increasing the number of iterations carried out by the NMCR, at the price of higher computational complexity.

4) The AP-ML and EM algorithms achieve similar accuracies, but the latter algorithm requires substantially lower computational complexity. Note also that the accuracy of these methods is limited by grid discretization and can be improved by increasing the search grid size or the number of iterations (at the price, however, of a substantial increase in the computational complexity).

5) The computational complexity of the 2D-FFTi, NMCR, EM and AP-ML algorithms is approximately 1.36, 1, 66, 8.76 and 9613 times higher than that of the 2D-FFT method, respectively.

Comparing the results of Fig. 5 with those shown in Fig. 4 leads to the following conclusions:

1) All the considered algorithms exhibit a general performance degradation with respect to the PSK case, especially at high SNRs, where the RMSEs deviate significantly from the CRLB. This deviation is primarily due to the non-uniform noise variance originating from the compensation of 16-QAM symbols (see (23)); in fact, this compromises the optimality of ML-based estimation techniques.

2) The NMCR algorithm outperforms the other techniques; at 5 dB, it achieves approximately a 20% better accuracy than both the EM and AP-ML algorithms in estimating range and velocity. Even if its accuracy does not follow the CRLB as closely as in the PSK case, it improves as the SNR increases.

Some numerical results referring to the accuracy achieved by all the considered algorithms in **S2** are shown in Fig. 6.

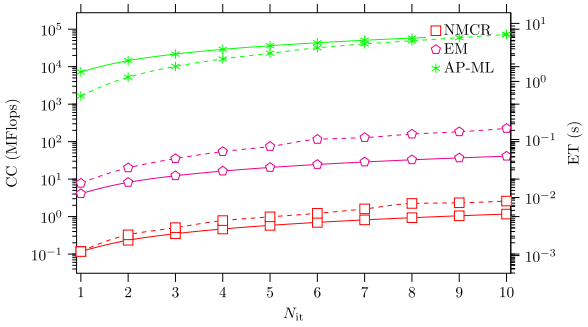

Fig. 9. Computational cost (solid lines), in MFLOPs, and execution time (dashed lines), in seconds, versus number of iterations, N_{it}, for the NMCR, EM and AP-ML algorithms. **S4** is considered.

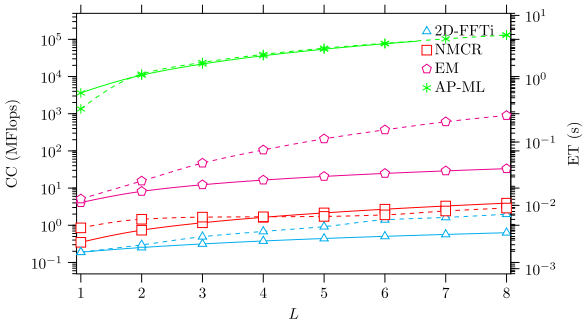

Fig. 10. Computational cost (solid lines), in MFLOPs, and execution time (dashed lines), in seconds, versus the overall number of targets, L, for the 2D-FFTi, NMCR, EM and AP-ML algorithms. **S5** is considered.

From these results, it is clearly inferred that the performance trend of all considered estimation techniques closely follows those already illustrated in **S1**. This is mainly due to the fact that the two targets detectable in **S2** are well separated in both range and Doppler domains. Note, however, that: 1) the CRLB values are slightly different from the ones shown for **S1**; 2) the NMCR algorithm achieves approximately a 35% better accuracy than the EM algorithm in range and velocity estimation for an SNR $= 5$ dB; 3) the EM algorithm marginally outperforms the AP-ML for the same grid size and overall number of refinement iterations for SNR $\in [3, 10]$ dB.

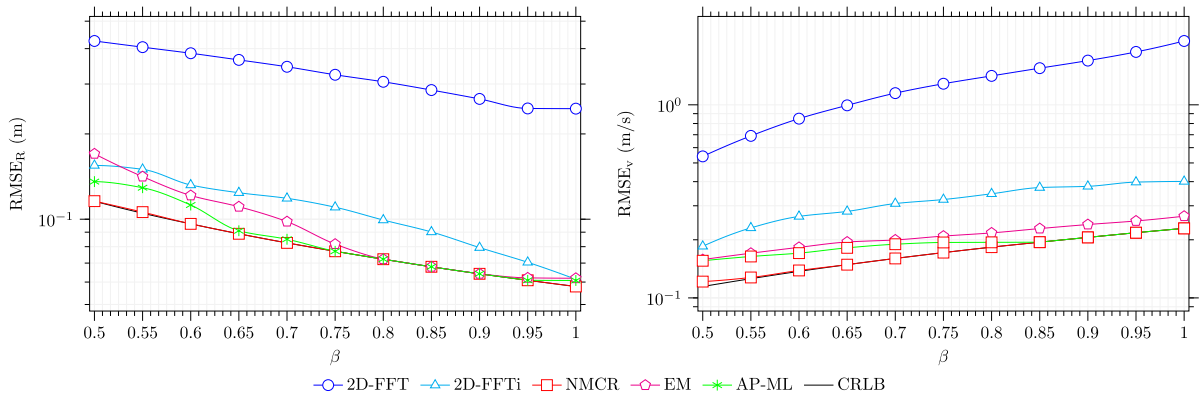

Fig. 11. Root mean square error performance achieved by 2D-FFT, 2D-FFTi, NMCR, EM and AP-ML algorithms, in range (left figure) and velocity estimation (right figure), versus compression factor $\beta \in [0.5, 1]$, for an SNR $= 0$ dB. **S6** is considered, and the CRLBs for range and velocity are also shown as references.

Note that the last result is due to the differences in the cost functions of the considered algorithms.

Some numerical results referring to **S3** are provided in Fig. 7, where the RMSE$_R$ and the RMSE$_v$ characterizing all the considered algorithms are shown. These results lead easily to the following conclusions:

1) The RMSE$_R$ curves for the 2D-FFT, 2D-FFTi and EM algorithms exhibit a floor for an SNR higher than -12 dB; this is due to the fact that the targets detectable in the considered scenario have close ranges.

2) The performance of the AP-ML and the NMCR algorithms in terms of RMSE$_R$ deviates from the CRLB for an SNR lower than that observed in **S2**; this can be related to the fact that targets in **S3** are more closely spaced than in **S2**. Moreover, the RMSE$_R$ performance of the NMCR algorithm shows an improvement of approximately 37% compared to that achieved by the AP-ML algorithm for an SNR $= 5$ dB.

3) The RMSE$_v$ curves for all the algorithms, except for that referring to the 2D-FFT method, are very close and tend to diverge from the CRLB since all the targets share the same velocity (so that estimation accuracy is substantially affected by spectral leakage).

Some numerical results referring to **S4** are provided in Fig. 8, where the dependence of RMSE$_R$ and RMSE$_v$ on the overall number of iterations is illustrated for all the considered iterative algorithms; it is assumed that $N_{\text{it}} \in \{1, 2, \ldots, 10\}$. These results evidence that:

1) At the considered SNR, the AP-ML, EM and NMCR algorithms achieve the CRLB after 4, 7 and 6 iterations, respectively, for range estimation, and after 4, 6 and 7 iterations, respectively, for velocity estimation.

2) The NMCR algorithm converges faster than the EM algorithm in range estimation, but the opposite occurs in speed estimation. This difference can be related to the distinct cost functions[19] involved in the estimation task of the two considered algorithms. It is important to observe that, since the NMCR algorithm stems from a ML approach, its capability to closely reach the CRLB at sufficiently high SNR provides strong evidence of reliable convergence.

3) As already mentioned above, since both the 2D-FFT and 2D-FFTi algorithms do not rely on multiple iterations to refine their range and velocity estimates, their RMSE performance is not shown in Fig. 8. However, for completeness, we mention that the RMSE values achieved by the 2D-FFT algorithm are approximately 0.92 m and 1.75 m/s for range and velocity, respectively, in **S4**.

The dependence of the complexity metrics, namely the *computational cost* (CC), expressed in MFLOPs, and the *execution time* (ET), in seconds, on the overall number of iterations is exemplified in Fig. 9, where the NMCR, EM and AP-ML algorithms have been considered; **S4** is considered in this case. These results lead to the following conclusions:

1) The CC results, based on our assessment of the computational complexity, are consistent with the ET curves.

2) The NMCR and AP-ML algorithms require 0.82 and $2.90 \cdot 10^3$ MFlops (these correspond to $6.4 \cdot 10^{-3}$ and 2.44 seconds), respectively, to achieve the CRLB in the considered scenario.[20] The last result is due to the fact that the AP-ML algorithm makes use of a grid to refine the frequency estimates and employs computationally intensive alternating projection steps.

3) The complexity of the EM algorithm stays in the middle.

The dependence of the CC and ET on the overall number of targets L is exemplified by Fig. 10. In this case, however, our results refer to the refinement step only for each of the considered algorithms; consequently, they do not take into account the complexity of the initialization step (i.e., of the 2D-FFT algorithm employed for this task). Note also that the CC and ET of the 2D-FFT algorithm remain constant at approximately 2.7 MFLOPs (see (44)) and 3.3 ms, respectively, for all the considered values of L. The last values can be easily added to the CC and ET appearing in Fig. 10 to assess, on average, the overall CC and ET of each technique within the considered range of L. From the results shown in Fig. 10 it is easily inferred that:

[19]Further simulation results, not shown here, have evidenced that the convergence behavior is also influenced by the choice of the algorithm parameters, such as the step size μ in the NMCR algorithm, and the mixing coefficients $\{\beta_l^{(i)}\}$ in the EM algorithm, although these effects depend on the specific scenario.

[20]Do not forget that, in **S4**, the NMCR and AP-ML algorithms require 7 and 4 iterations, respectively, to achieve the CRLB.

1) The 2D-FFTi and AP-ML algorithms exhibit the lowest computational complexity and the highest one, respectively.

2) The NMCR and EM algorithms fall in between, but the NMCR algorithm exhibits a noticeably lower complexity than the EM algorithm.

Finally, some results unveiling the impact of the compression factor on the RMSE performance are illustrated in Fig. 11, where $\beta \in [0.5, 1]$ is assumed. These results show that:

1) The accuracy in range estimation improves as β increases, but the opposite occurs for speed estimation. This result originates from the fact that a smaller β results in a reduced spacing between normalized delays of the considered targets, but in an increased spacing between their normalized Doppler frequencies. These effects are also reflected in the trend of the CRLB, which decreases for range estimation and increases for Doppler estimation as β becomes larger.

2) The NMCR accuracy is very close to the CRLB for both range and velocity at the given SNR and for all the considered values of β. When $\beta = 0.5$, the NMCR algorithm achieves approximately 15% and 20% better accuracy than the AP-ML algorithm in estimating range and velocity, respectively.

3) The AP-ML and EM approach algorithms the CRLB for $\beta \in [0.75, 0.95]$ in range estimation. Additionally, the AP-ML performance is comparable to that of the NMCR algorithm in velocity estimation for a β greater than 0.85.

V. Conclusion

In this manuscript, the sensing problem for SEFDM signaling with CP has been formulated and a novel iterative method, based on a ML approach, has been developed to solve it. Our method, dubbed NMCR, is initialized by means of the 2D periodogram technique and exploits a novel 2D frequency refinement procedure. Our numerical results show that, in various scenarios, the NMCR method achieves a better accuracy-complexity trade-off than other alternatives available in the technical literature. In particular, in our simulations, the NMCR algorithm has shown a superior accuracy, with an improvement ranging from 15% to 50% at high SNR values, and maintains its leading performance even at low compression factors, outperforming the other considered methods.

Our analysis has also unveiled some fundamental trade-offs inherent to SEFDM signaling. In particular, it has shown that, on the one hand, the use of a CP simplifies channel estimation and mitigates ISI, but at the cost of a SE reduction. On the other hand, reducing the subcarrier spacing improves SE, but significantly increases ICI, making the SEFDM-based target estimation problem more challenging even with constant-modulus constellations such as PSK.

Moreover, our analysis has evidenced that, similarly to OFDM, SEFDM exhibits poor performance over highly time-varying channels; this may limit its applicability to very high-Doppler scenarios and when the RX side is affected by non-Gaussian noise.

Possible directions for future research include: 1) the extension of the proposed framework to MIMO radar architectures, enabling joint range–Doppler–angle estimation and full target localization; 2) hybrid waveform design for ISAC; 3) the adoption of alternative non-orthogonal modulation formats that are more robust to doubly-selective channels.

Appendix

A. Gradient and Hessian of the LL Function

In this appendix, the derivation of the gradient (37) and of the Hessian matrix (38) for the cost function $\mathcal{L}$ (35) is sketched. Before doing so, some basic properties of the Dirac vectors as well as of the stacking operations are illustrated. To this aim, we define: a) the L-dimensional vectors $\mathbf{x} \triangleq [x_0, x_1, \ldots, x_{L-1}]^T$, $\mathbf{y} \triangleq [y_0, y_1, \ldots, y_{L-1}]^T$ and $\mathbf{z} \triangleq [z_0, z_1, \ldots, z_{L-1}]^T$(the lth element is denoted x_l, y_l and z_l, respectively); b) the $L \times L$ matrix $\mathbf{A} \triangleq [a_{l,l'}]$ (its (l, l')th element is denoted $a_{l,l'}$); c) the L-dimensional vector $\boldsymbol{\delta}_{L,l}$, called *Dirac vector*, having its lth element equal to unity and its remaining $(L-1)$ elements equal to zero. Given these definitions, the following properties can be proved (here, **P***i* indicates the ith property):

- **P1**:$\mathbf{x}^T \boldsymbol{\delta}_{L,l} = x_l$
- **P2**:$\boldsymbol{\delta}_{L,l}\, \mathbf{A}\, \boldsymbol{\delta}_{L,l'} = a_{l,l'}$
- **P3**: if $z_l = x_l\, y_l$ for any l, then $\mathbf{z} = \mathbf{x} \odot \mathbf{y}$
- **P4**: if $a_{l,l'} = x_l\, y_{l'}$, for any l and l', then $\mathbf{A} = \mathbf{x}\mathbf{y}^T$

Our derivations start with substituting the expression of $\mathbf{h}(\cdot,\cdot,\cdot)$ (25) in the RHS of (35) and evaluating the partial derivative of the resulting expression with respect to the scalar frequency $\tilde{F}_{\tau_l}$ (with $l = 0, 1, \ldots, L-1$); this yields

$$\frac{\partial \mathcal{L}}{\partial \tilde{f}_{\tau_l}} = -2\Re\Big\{\tilde{\mathbf{a}}^H \boldsymbol{\delta}_{L,l}\, \boldsymbol{\delta}_{L,l}^T\, \dot{\mathbf{B}}_{\tilde{\mathbf{f}}_\tau}^H \big(\hat{\mathbf{h}} - \mathbf{B}\tilde{\mathbf{a}}\big)\Big\}, \tag{47}$$

where $\dot{\mathbf{B}}_{\tilde{\mathbf{f}}_\tau}^H$ is an $(MN) \times L$ matrix, whose lth column contains the partial derivative of the lth column of $\mathbf{B}$ (see (26) with $(\mathbf{f}_\tau, \mathbf{f}_\nu) = (\tilde{\mathbf{f}}_\tau, \tilde{\mathbf{f}}_\nu)$), with respect to $\tilde{f}_{\tau_l}$. The partial derivative of $\mathcal{L}$ (35) with respect to the scalar frequency $\tilde{f}_{\nu_l}$ (with $l = 0, 1, \ldots, L-1$) can be computed in a similar way; this results in

$$\frac{\partial \mathcal{L}}{\partial \tilde{f}_{\nu_l}} = -2\Re\Big\{\tilde{\mathbf{a}}^H \boldsymbol{\delta}_{L,l}\, \boldsymbol{\delta}_{L,l}^T\, \dot{\mathbf{B}}_{\tilde{\mathbf{f}}_\nu}^H \big(\hat{\mathbf{h}} - \mathbf{B}\tilde{\mathbf{a}}\big)\Big\}, \tag{48}$$

where $\dot{\mathbf{B}}_{\tilde{\mathbf{f}}_\nu}$ is an $(MN) \times L$ matrix, whose lth column contains the partial derivative of the lth column of $\mathbf{B}$ (see (26) with $(\mathbf{f}_\tau, \mathbf{f}_\nu) = (\tilde{\mathbf{f}}_\tau, \tilde{\mathbf{f}}_\nu)$), with respect to $\tilde{f}_{\nu_l}$. Given the partial derivatives in (47) and (48), the gradient vector $\nabla_{\mathcal{L}}(\tilde{\mathbf{a}}, \tilde{\mathbf{f}})$ (having length equal to $2L$) can be obtained, since

$$\nabla_{\mathcal{L}}(\tilde{\mathbf{a}}, \tilde{\mathbf{f}}) \triangleq \left[\frac{\partial \mathcal{L}}{\partial \tilde{f}_{\tau_0}}, \frac{\partial \mathcal{L}}{\partial \tilde{f}_{\tau_1}}, \ldots, \frac{\partial \mathcal{L}}{\partial \tilde{f}_{\tau_{L-1}}}, \frac{\partial \mathcal{L}}{\partial \tilde{f}_{\nu_0}}, \frac{\partial \mathcal{L}}{\partial \tilde{f}_{\nu_1}}, \ldots, \frac{\partial \mathcal{L}}{\partial \tilde{f}_{\nu_{L-1}}}\right]^T. \tag{49}$$

Exploiting the property **P1** in both (47) and (48) and the property **P3** in (49) easily leads to (37).

The evaluation of the $(2L) \times (2L)$ Hessian matrix $\ddot{\mathbf{H}}_{\mathcal{L}}(\tilde{\mathbf{a}}, \tilde{\mathbf{f}})$ requires computing the partial derivatives of $\mathcal{L}$ (35) with respect to the couple of variables $(\tilde{f}_{\tau_l}, \tilde{f}_{\tau_{l'}})$, $(\tilde{f}_{\tau_l}, \tilde{f}_{\nu_{l'}})$, $(\tilde{f}_{\nu_l}, \tilde{f}_{\tau_{l'}})$ and $(\tilde{f}_{\nu_l}, \tilde{f}_{\nu_{l'}})$. Following the same line of reasoning as the one illustrated for the evaluation of the gradient of $\mathcal{L}$, it can be easily shown that

$$\begin{aligned}\frac{\partial^2 \mathcal{L}}{\partial \tilde{f}_{\tau_l} \partial \tilde{f}_{\tau_{l'}}} = &-2\Re\Big\{\tilde{\mathbf{a}}^H \boldsymbol{\delta}_{L,l}\, \boldsymbol{\delta}_{L,l'}^T\, \ddot{\mathbf{B}}_{\tilde{\mathbf{f}}_\tau, \tilde{\mathbf{f}}_\tau}^H \big(\hat{\mathbf{h}} - \mathbf{B}\tilde{\mathbf{a}}\big)\Big\} \\ &+ 2\Re\Big\{\tilde{\mathbf{a}}^H \boldsymbol{\delta}_{L,l}\, \boldsymbol{\delta}_{L,l}^T\, \dot{\mathbf{B}}_{\tilde{\mathbf{f}}_\tau}^H\, \dot{\mathbf{B}}_{\tilde{\mathbf{f}}_\tau}\, \boldsymbol{\delta}_{L,l'}\, \boldsymbol{\delta}_{L,l'}^T\, \tilde{\mathbf{a}}\Big\},\end{aligned} \tag{50}$$

$$\frac{\partial^2 \mathcal{L}}{\partial \tilde{f}_{\tau_l} \partial \tilde{f}_{\nu_{l'}}} = -2\Re\Big\{\tilde{\mathbf{a}}^H \boldsymbol{\delta}_{L,l}\, \boldsymbol{\delta}_{L,l'}^T\, \ddot{\mathbf{B}}^H_{\tilde{\mathbf{f}}_\tau, \tilde{\mathbf{f}}_\nu} (\hat{\mathbf{h}} - \mathbf{B}\tilde{\mathbf{a}})\Big\} + 2\Re\Big\{\tilde{\mathbf{a}}^H \boldsymbol{\delta}_{L,l}\, \boldsymbol{\delta}_{L,l}^T\, \dot{\mathbf{B}}^H_{\tilde{\mathbf{f}}_\tau} \dot{\mathbf{B}}_{\tilde{\mathbf{f}}_\nu} \boldsymbol{\delta}_{L,l'}\, \boldsymbol{\delta}_{L,l'}^T\, \tilde{\mathbf{a}}\Big\}, \quad (51)$$

$$\frac{\partial^2 \mathcal{L}}{\partial \tilde{f}_{\nu_l} \partial \tilde{f}_{\tau_{l'}}} = -2\Re\Big\{\tilde{\mathbf{a}}^H \boldsymbol{\delta}_{L,l}\, \boldsymbol{\delta}_{L,l'}^T\, \ddot{\mathbf{B}}^H_{\tilde{\mathbf{f}}_\nu, \tilde{\mathbf{f}}_\tau} (\hat{\mathbf{h}} - \mathbf{B}\tilde{\mathbf{a}})\Big\} + 2\Re\Big\{\tilde{\mathbf{a}}^H \boldsymbol{\delta}_{L,l}\, \boldsymbol{\delta}_{L,l}^T\, \dot{\mathbf{B}}^H_{\tilde{\mathbf{f}}_\nu} \dot{\mathbf{B}}_{\tilde{\mathbf{f}}_\tau} \boldsymbol{\delta}_{L,l'}\, \boldsymbol{\delta}_{L,l'}^T\, \tilde{\mathbf{a}}\Big\} \quad (52)$$

and

$$\frac{\partial^2 \mathcal{L}}{\partial \tilde{f}_{\nu_l} \partial \tilde{f}_{\nu_{l'}}} = -2\Re\Big\{\tilde{\mathbf{a}}^H \boldsymbol{\delta}_{L,l}\, \boldsymbol{\delta}_{L,l'}^T\, \ddot{\mathbf{B}}^H_{\tilde{\mathbf{f}}_\nu, \tilde{\mathbf{f}}_\nu} (\hat{\mathbf{h}} - \mathbf{B}\tilde{\mathbf{a}})\Big\} + 2\Re\Big\{\tilde{\mathbf{a}}^H \boldsymbol{\delta}_{L,l}\, \boldsymbol{\delta}_{L,l}^T\, \dot{\mathbf{B}}^H_{\tilde{\mathbf{f}}_\nu} \dot{\mathbf{B}}_{\tilde{\mathbf{f}}_\nu} \boldsymbol{\delta}_{L,l'}\, \boldsymbol{\delta}_{L,l'}^T\, \tilde{\mathbf{a}}\Big\}. \quad (53)$$

Given equations (50)-(53), the $(2L) \times (2L)$ Hessian matrix of $\ddot{\mathbf{H}}_{\mathcal{L}}(\tilde{\mathbf{a}}, \tilde{\mathbf{f}})$ can be easily put in the form (38), by exploiting:

1) **P1** for all the terms $\tilde{\mathbf{a}}^H \boldsymbol{\delta}_{L,l}$ and $\boldsymbol{\delta}_{L,l'}^T \tilde{\mathbf{a}}$ in (50)-(53);

2) **P1** for the terms $\boldsymbol{\delta}_{L,l'}^T \ddot{\mathbf{B}}^H_{\tilde{\mathbf{f}}_\tau, \tilde{\mathbf{f}}_\tau} \mathbf{y}$, $\boldsymbol{\delta}_{L,l'}^T \ddot{\mathbf{B}}^H_{\tilde{\mathbf{f}}_\tau, \tilde{\mathbf{f}}_\nu} \mathbf{y}$, $\boldsymbol{\delta}_{L,l'}^T \ddot{\mathbf{B}}^H_{\tilde{\mathbf{f}}_\nu, \tilde{\mathbf{f}}_\tau} \mathbf{y}$ and $\boldsymbol{\delta}_{L,l'}^T \ddot{\mathbf{B}}^H_{\tilde{\mathbf{f}}_\nu, \tilde{\mathbf{f}}_\nu} \mathbf{y}$, in (50), (51), (52) and (53), respectively (here, $\mathbf{y} \triangleq \hat{\mathbf{h}} - \mathbf{B}\tilde{\mathbf{a}}$);

3) **P2** for the terms $\boldsymbol{\delta}_{L,l}^T \dot{\mathbf{B}}^H_{\tilde{\mathbf{f}}_\tau} \dot{\mathbf{B}}_{\tilde{\mathbf{f}}_\tau} \boldsymbol{\delta}_{L,l'}$, $\boldsymbol{\delta}_{L,l}^T \dot{\mathbf{B}}^H_{\tilde{\mathbf{f}}_\tau} \dot{\mathbf{B}}_{\tilde{\mathbf{f}}_\nu} \boldsymbol{\delta}_{L,l'}$, $\boldsymbol{\delta}_{L,l}^T \dot{\mathbf{B}}^H_{\tilde{\mathbf{f}}_\nu} \dot{\mathbf{B}}_{\tilde{\mathbf{f}}_\tau} \boldsymbol{\delta}_{L,l'}$ and $\boldsymbol{\delta}_{L,l}^T \dot{\mathbf{B}}^H_{\tilde{\mathbf{f}}_\nu} \dot{\mathbf{B}}_{\tilde{\mathbf{f}}_\nu} \boldsymbol{\delta}_{L,l'}$, in (50), (51), (52) and (53), respectively.

4) **P3** and **P4** in the resulting expressions.

B. Derivation of the Cramér-Rao Lower Bounds

In this appendix, the CRLB for the joint estimation of the complex gains $\mathbf{a}$ (29), the normalized delays $\mathbf{f}_\tau$ (30) and the normalized Doppler frequencies $\mathbf{f}_\nu$ (31) associated with L targets is derived. Note that the CRLBs referring to the considered estimation problem have already been derived for OFDM-based radar systems (e.g., see [12]); however, as far we know, the same derivation for SEFDM-based co-located radar systems has never appeared so far.

First of all, let us consider the model (24), that refers to L distinct targets, and define the trial vectors $\tilde{\mathbf{a}}$, $\tilde{\mathbf{f}}_\tau$ and $\tilde{\mathbf{f}}_\nu$ in a similar way as $\mathbf{a}$ (29), $\mathbf{f}_\tau$ (30) and $\mathbf{f}_\nu$ (31), respectively.

The CRLBs we are interested in refer to the ML estimation problem (34). If we assume that the elements of the noise vector $\breve{\mathbf{w}}$, in (24), are Gaussian, mutually independent and have zero mean and variance σ_{w}^2, the CRLBs of all the parameters of interest are represented by the diagonal elements of the matrix

$$\mathbf{V} = \sigma_{\mathbf{w}}^2 \boldsymbol{\Phi}^{-1}, \quad (54)$$

where

$$\boldsymbol{\Phi} \triangleq [\Phi_{i,j}] = 2\Re\left\{\frac{\partial \tilde{\mathbf{h}}}{\partial \tilde{\mathbf{f}}}\left(\frac{\partial \tilde{\mathbf{h}}}{\partial \tilde{\mathbf{f}}}\right)^H\right\} \quad (55)$$

is the $(2L) \times (2L)$ *Fisher information matrix* (FIM) computed for the (MN)-dimensional row vector $\tilde{\mathbf{h}} \triangleq \mathbf{h}^T(\tilde{\mathbf{a}}, \tilde{\mathbf{f}}_\tau, \tilde{\mathbf{f}}_\nu)$ (see (25)). Note that, in (55), $\tilde{\mathbf{f}} \triangleq [\tilde{\mathbf{f}}_\tau^T, \tilde{\mathbf{f}}_\nu^T]^T$ is a $(2L)$-dimensional column vector. Moreover, it is not difficult to prove that

$$\frac{\partial \tilde{\mathbf{h}}}{\partial \tilde{\mathbf{f}}} = [\mathbf{P}, \mathbf{Q}]^T, \quad (56)$$

where $\mathbf{P} \triangleq [\tilde{\mathbf{P}}_0, \tilde{\mathbf{P}}_1, \ldots, \tilde{\mathbf{P}}_{L-1}]$ and $\mathbf{Q} \triangleq [\tilde{\mathbf{Q}}_0, \tilde{\mathbf{Q}}_1, \ldots, \tilde{\mathbf{Q}}_{L-1}]$ are $(MN) \times L$ matrices containing the partial derivatives with respect to the delay and Doppler parameters $\{f_{\tau_l}\}$ and $\{f_{\nu_l}\}$, respectively. The lth column of $\mathbf{P}$ and $\mathbf{Q}$ can be expressed as (see (28))

$$\tilde{\mathbf{P}}_l = -\breve{a}_l \left(\boldsymbol{\Upsilon}_N \odot \bar{\mathbf{b}}_N^*(f_{\tau_l})\right) \circledast \bar{\mathbf{b}}_M(f_{\nu_l}), \quad (57)$$

$$\tilde{\mathbf{Q}}_l = \breve{a}_l\, \bar{\mathbf{b}}_N^*(f_{\tau_l}) \circledast \left(\boldsymbol{\Upsilon}_M \odot \bar{\mathbf{b}}_M(f_{\nu_l})\right), \quad (58)$$

respectively; finally, $\boldsymbol{\Upsilon}_X \triangleq [0, j2\pi, \ldots, j2\pi(X-1)]^T$, for any integer X.

It is worth emphasizing that the FIM in (55) includes cross-terms requiring the evaluation of partial derivatives with respect to heterogeneous parameters. In fact, substituting the RHS of (56) in that of (55) yields

$$\boldsymbol{\Phi} = 2\Re\left\{\begin{bmatrix}\mathbf{P}^H\mathbf{P} & \mathbf{P}^H\mathbf{Q} \\ \mathbf{Q}^H\mathbf{P} & \mathbf{Q}^H\mathbf{Q}\end{bmatrix}\right\} \quad (59)$$

The presence of the above-mentioned cross-terms results in a dependence of the last matrix, and consequently, of the matrix $\mathbf{V}$ (54), on the relative spacing between the normalized delays and Doppler frequencies of the L targets. Consequently, even when the actual range and Doppler values of the targets are kept fixed, any change in the compression factor β (which scales the normalized frequency grid) affects the values of the normalized frequencies $\mathbf{f}_\tau$ and $\mathbf{f}_\nu$, and thus modifies the structure of the FIM and the resulting CRLBs. This justifies the β-dependent behavior of the considered estimation bounds, as discussed in the main text. In our work, all the above-mentioned CRLBs have been evaluated numerically on the basis of (54)-(59); in doing so, the expected value of each random variable in the set $\{(\breve{a}_l, f_{\tau_l}, f_{\nu_l});\, l = 0, 1, \ldots, L-1\}$ has been used.

REFERENCES

[1] J. A. Zhang et al., "An overview of signal processing techniques for joint communication and radar sensing," *IEEE J. Sel. Topics Signal Process.*, vol. 15, no. 6, pp. 1295–1315, Nov. 2021.

[2] Z. Wei et al., "Integrated sensing and communication signals toward 5G-A and 6G: A survey," *IEEE Internet Things J.*, vol. 10, no. 13, pp. 11068–11092, Jul. 2023.

[3] I. Darwazeh and M. Rodrigues, "A spectrally efficient frequency division multiplexing based communications system," in *Proc. 8th Int. OFDM-Workshop (InOWo)*, Sep. 2003, pp. 70–74.

[4] S. Isam, I. Kanaras, and I. Darwazeh, "A truncated SVD approach for fixed complexity spectrally efficient FDM receivers," in *Proc. IEEE Wireless Commun. Netw. Conf.*, Mar. 2011, pp. 1584–1589.

[5] S. Isam and I. Darwazeh, "Design and performance assessment of fixed complexity spectrally efficient FDM receivers," in *Proc. IEEE 73rd Veh. Technol. Conf. (VTC Spring)*, May 2011, pp. 1–5.

[6] B. Yu et al., "Channel equalisation and data detection for SEFDM over frequency selective fading channels," *IET Commun.*, vol. 12, no. 18, pp. 2315–2323, Oct. 2018.

[7] Y. Ma, F. Tian, N. Wu, B. Li, and X. Ma, "A low-complexity receiver for multicarrier faster-than-Nyquist signaling over frequency selective channels," *IEEE Commun. Lett.*, vol. 24, no. 1, pp. 81–85, Jan. 2020.

[8] M. Mirabella, P. Di Viesti, and G. M. Vitetta, "A novel message passing algorithm for soft-output detection in faster-than-Nyquist multicarrier systems," in *Proc. IEEE 26th Int. Workshop Signal Process. Artif. Intell. Wireless Commun. (SPAWC)*, Jul. 2025, pp. 1–5.

[9] C. Sturm and W. Wiesbeck, "Waveform design and signal processing aspects for fusion of wireless communications and radar sensing," *Proc. IEEE*, vol. 99, no. 7, pp. 1236–1259, Jul. 2011.

[10] S. Mercier, S. Bidon, D. Roque, and C. Enderli, "Comparison of correlation-based OFDM radar receivers," *IEEE Trans. Aerosp. Electron. Syst.*, vol. 56, no. 6, pp. 4796–4813, Dec. 2020.

[11] L. Zheng and X. Wang, "Super-resolution delay-Doppler estimation for OFDM passive radar," *IEEE Trans. Signal Process.*, vol. 65, no. 9, pp. 2197–2210, May 2017.

[12] R. Xie, D. Hu, K. Luo, and T. Jiang, "Performance analysis of joint range-velocity estimator with 2D-MUSIC in OFDM radar," *IEEE Trans. Signal Process.*, vol. 69, pp. 4787–4800, 2021.
[13] U. K. Singh, R. Mitra, V. Bhatia, and A. K. Mishra, "Target range estimation in OFDM radar system via kernel least mean square technique," in *Proc. Int. Conf. Radar Syst. (Radar)*, 2017, p. 44.
[14] F. Zhang, Z. Zhang, W. Yu, and T.-K. Truong, "Joint range and velocity estimation with intrapulse and intersubcarrier Doppler effects for OFDM-based RadCom systems," *IEEE Trans. Signal Process.*, vol. 68, pp. 662–675, 2020.
[15] Y. L. Sit, C. Sturm, and T. Zwick, "Doppler estimation in an OFDM joint radar and communication system," in *Proc. German Microw. Conf.*, Mar. 2011, pp. 1–4.
[16] M. Mirabella, P. D. Viesti, A. Davoli, and G. M. Vitetta, "Deterministic signal processing techniques for OFDM-based radar sensing: An overview," *IEEE Access*, vol. 11, pp. 68872–68889, 2023.
[17] M. Mirabella, P. D. Viesti, and G. M. Vitetta, "On the use of a two-dimensional cyclic prefix in OTFS modulation and its implications," *IEEE Open J. Commun. Soc.*, vol. 5, pp. 3340–3367, 2024.
[18] B. Ottersten, M. Viberg, P. Stoica, and A. Nehorai, "Exact and large sample maximum likelihood techniques for parameter estimation and detection in array processing," in *Radar Array Processing*. Cham, Switzerland: Springer, 1993, pp. 99–151.
[19] M. Mirabella, P. Di Viesti, and G. M. Vitetta, "Deterministic algorithms for four-dimensional imaging in colocated MIMO OFDM-based radar systems," *IEEE Open J. Commun. Soc.*, vol. 4, pp. 1516–1543, 2023.
[20] D. A. Shnidman, "Expanded swerling target models," *IEEE Trans. Aerosp. Electron. Syst.*, vol. 39, no. 3, pp. 1059–1069, Jul. 2003.

Michele Mirabella (Member, IEEE) received the B.S. degree (cum laude) in electronic engineering from the University of Modena and Reggio Emilia, Italy, in 2019, and the M.S. degree (cum laude) in electronic engineering from the University of Bologna in 2021, and the Ph.D. degree from the University of Modena and Reggio Emilia in January 2025. His Ph.D. program titled "Vehicle-to-everything (V2X) Communications for Green and Reliable Intelligent Transportation Systems." He is currently a Research Fellow with the University of Modena and Reggio Emilia. His main research interests lie in the areas of digital signal processing for radar systems and joint communication and sensing systems. He was recipient of the Best Paper Awards in the IEEE Joint Communications and Sensing Symposium 2026.

Pasquale Di Viesti (Member, IEEE) received the bachelor's and master's degrees (cum laude) in electronic engineering from the University of Modena and Reggio Emilia, Italy, in 2016 and 2018, respectively, and the Ph.D. degree in automotive for an intelligent mobility from the University of Bologna in 2021. He is currently a Post-Doctoral Research Fellow with the University of Modena and Reggio Emilia. His main research interests lie in the area of statistical signal processing, multiple-input–multiple-output (MIMO) radars, and joint communication and sensing systems.

Christos Masouros (Fellow, IEEE) received the Diploma degree in electrical and computer engineering from the University of Patras, Greece, in 2004, and the M.Sc. (by research) and Ph.D. degrees in electrical and electronic engineering from the University of Manchester, U.K., in 2006 and 2009, respectively. In 2008, he was a Research Intern with Philips Research Labs, U.K., working on the LTE standards. From 2009 to 2010, he was a Research Associate with the University of Manchester. From 2010 to 2012, he was a Research Fellow with Queen's University Belfast. In 2012, he joined University College London, as a Lecturer. He has held a Royal Academy of Engineering Research Fellowship from 2011 to 2016. Since 2019, he has been a Full Professor of signal processing and wireless communications with the Information and Communication Engineering Research Group, Department of Electrical and Electronic Engineering, Institute for Communications and Connected Systems, University College London. From 2018 to 2022, he was the Project Coordinator of the €4.2m EU H2020 ITN project PAINLESS, involving 12 EU partner universities and industries, toward energy-autonomous networks. From 2024 to 2028, he will be the Scientific Coordinator of the €2.7m EU H2020 DN project ISLANDS, involving 19 EU partner universities and industries, toward next generation vehicular networks. His research interests lie in the field of wireless communications and signal processing, with particular focus on green communications, large-scale antenna systems, integrated sensing and communications, interference mitigation techniques for MIMO, and multicarrier communications. He is a fellow of the Institute of Electronic Engineers (IET), the Artificial Intelligence Industry Alliance (AIIA), and Asia-Pacific Artificial Intelligence Association (AAIA). He was a recipient of the 2024 IEEE SPS Best Paper Award, the 2024 IEEE SPS Donald G. Fink Overview Paper Award, the 2023 IEEE ComSoc Stephen O. Rice Prize, and the Best Paper Awards in the IEEE GlobeCom 2015 and IEEE WCNC 2019 conferences. He was a co-recipient of the 2021 IEEE SPS Young Author Best Paper Award. His work on ISAC has been featured in the World Economic Forum's report on the top ten emerging technologies. He is a Founding Member and the Vice-Chair of the IEEE Emerging Technology Initiative on Integrated Sensing and Communications (SAC); and the Chair of the IEEE SPS ISAC Technical Working Group, the IEEE Green Communications and Computing Technical Committee, and a Special Interest Group on Green ISAC. He is a member of the IEEE Standards Association Working Group on ISAC performance metrics and a Founding Member of ETSI ISG on ISAC. He is the TPC Chair of IEEE ICC 2024 Selected Areas in Communications (SAC) Track on ISAC, the Chair of the IEEE PIMRC2024 Track 1 on PHY and Fundamentals and the "Integrated Imaging and Communications" stream in IEEE CISA 2024, and the TPC Co-Chair of IEEE VTC 2025. He has been recognized as an Exemplary Editor for IEEE COMMUNICATIONS LETTERS and an Exemplary Reviewer for IEEE TRANSACTIONS ON COMMUNICATIONS. He is an Area Editor of IEEE TRANSACTIONS ON WIRELESS COMMUNICATIONS and the Editor-at-Large of IEEE OPEN JOURNAL OF THE COMMUNICATIONS SOCIETY. He has been an Editor of IEEE TRANSACTIONS ON COMMUNICATIONS, IEEE TRANSACTIONS ON WIRELESS COMMUNICATIONS, and IEEE OPEN JOURNAL OF SIGNAL PROCESSING; an Associate Editor of IEEE COMMUNICATIONS LETTERS; and a Guest Editor of several IEEE JOURNAL ON SELECTED TOPICS IN SIGNAL PROCESSING special issues. He is an IEEE ComSoc Distinguished Lecturer from 2024 to 2025.

Giorgio M. Vitetta (Senior Member, IEEE) received the Dr.-Ing. degree (cum Laude) in electronic engineering and the Ph.D. degree from the University of Pisa, Italy, in 1990 and 1994, respectively. He has been a Full Professor of telecommunications with the University of Modena and Reggio Emilia since 2001. He has co-authored more than 100 papers published on international journals and the proceedings of international conferences. He has co-authored the book *Wireless Communications: Algorithmic Techniques* (John Wiley, 2013). His main research interests lie in the broad area of wireless and wired data communications, localization systems, and MIMO radars. He has served as an Associate Editor and an Area Editor for IEEE TRANSACTIONS ON COMMUNICATIONS and an Associate Editor for IEEE WIRELESS COMMUNICATIONS LETTERS and IEEE TRANSACTIONS ON WIRELESS COMMUNICATIONS.

Open Access funding provided by 'Università degli Studi di Modena e Reggio Emilia 2025–2027 Deposit Account' within the CRUI CARE Agreement